[Brunel University of London]

ME5692 Group Project Design and Development of a Brunel Hexapod Robot

Supervised by: Dr. Mingfeng Wang

Mingi Choi	2446225
Roro Mohammadi	2107729
Anbit Chhetri	1914191
Hamza Al-Siyabi	2429643
Huimin Wang	2407446

List of Contents

1. Introduction

The demand for adaptable, resilient robotic systems capable of traversing variable terrain and manipulating physical objects continues to rise across sectors such as disaster response, agriculture, and exploration. Conventional wheeled and tracked systems lack the ability to effectively negotiate irregular environments, which has led to increased research into biologically inspired legged robots. Among these, hexapods offer intrinsic stability and locomotion redundancy through six-legged support, making them ideal candidates for applications requiring both mobility and manipulation (Ting et al., 1994; Altendorfer et al., 2001).

This project aims to enhance an existing hexapod platform developed at Brunel University by incorporating modular engineering principles and a Unified-Prismatic-Universal (UPU) leg architecture. The goal is to deliver a lightweight, reprogrammable robotic system that maintains balance and functionality across uneven terrain while offering manipulability via its terminal link. Unlike prior rigid systems, this robot features modular subsystems that are individually designed, analysed, and integrated to collectively address terrain adaptability, mechanical stress resilience, energy efficiency, and functional versatility.

Despite the promise of hexapod platforms, many existing solutions remain constrained by rigid architectures, limited terrain responsiveness, and a lack of multifunctionality. These limitations pose a significant challenge in real-world deployment scenarios where terrain irregularity, energy constraints, and functional flexibility cannot be compromised. To address these shortcomings, the current project introduces an enhanced hexapod design that prioritises adaptability, subsystem modularity, and simulation-driven development.

Project Aim:

To design, simulate, and validate a modular hexapod robotic system capable of adaptive terrain traversal and dual-role manipulation, using a Universal-Prismatic-Universal (UPU) leg chain architecture, simulation-informed subsystem development, and real-time gait stability feedback.

Project Objectives:

- To optimise each subsystem (upper platform, prismatic link, universal joint, end effector, gait control) based on terrain-specific simulation metrics.
- To integrate individual subsystems into a unified mechanical and control architecture.

- To validate system-level performance through terrain-aware gait testing and FEA-driven structural analysis.

Each group member focused on a specific subsystem, contributing to a unified hexapod capable of walking, grasping, and adjusting to unpredictable terrain conditions. The robot includes five primary subsystems:

Prismatic Link: It is a key part in controlling the length in the vertical direction in the Hexapod robot leg mechanism, and structural stability plays a critical role in load transmission and posture maintenance. To secure the part's structural reliability and select a material suitable for a 3D printing-based prototype, FEA analysis and material optimisation under static load were performed.

First, the mass data of each component was shared with the team members to calculate the load of the entire robot, and based on this, the load conditions under the work-case scenario were defined. After that, FEA was conducted on six 3D printing materials, including metallic and polymeric materials such as AlSi10Mg, 17-4PH, Ti-6Al-4V, and ABS-Like White, PA614-GS, and PA650. For each material, von Mises stress, maximum displacement, and overall strain were analysed to compare and evaluate the structural performance. Furthermore, the WDM (Weighted Decision Matrix) technique considered practical factors such as mass, manufacturing complexity, and cost efficiency, not just a simple mechanical performance comparison. As a result of the evaluation, AlSi10Mg material was derived as an optimal material by satisfying high rigidity, low strain, and the highest reliability compared to the initial investment.

In addition, practical material selection guidelines for 3D printing prototypes were also presented, allowing them to be used as a standard for future design optimisation and prototype production for the same purpose.

Upper Platform: Responsible for interfacing all six legs and distributing load evenly across the system. The redesigned platform features symmetric leg arrangements on a hexagonal layout, minimising rotational torque during locomotion. Through SolidWorks-based motion analysis and CAD integration studies, the platform was structurally optimised to accommodate servo motors, wiring channels, and a low centre of mass. The addition of a vertical offset between actuator mountings and the CoM helped reduce toppling moments during inclined traversal.

End Effector: Inspired by the Fin Ray effect observed in fish fins, the end effector enables dual-mode functionality: object grasping and stable support. Using ANSYS simulations across twelve design variations, the structure was optimised by altering rib angle, contact /

opposite side wall thicknesses, and material stiffness (Elgeneidy et al., 2020; Pledger and Wang, 2022; Suder et al., 2021; Antunes et al., 2024). Thermoplastic polyurethane (TPU A85 and A95) was tested, with results showing that rib angle asymmetry and rear wall thickening improved contact area and load support while maintaining deformability. This dual-role implementation supports both manipulation and locomotion requirements, critical for mission adaptability.

Shoulder Joint (Universal Joint): The hexapod's upper limb interface was optimised through nonlinear finite element analysis using SolidWorks. Initial PLA designs were replaced by AZ31B magnesium alloy due to its superior strength-to-weight ratio and fatigue properties (Yadav and Jain, 2021). The geometry was iteratively refined to reduce stress concentrations using fillet radius enhancement and ribbed internal supports (Altendorfer et al., 2001). Peak Von Mises stress was reduced by 48%, while displacement dropped by 98.6%, ensuring stability during pitch and yaw motion across rugged terrain.

Gait Simulation and Terrain Adaptability: A custom MATLAB simulation framework was developed to test ripple, wave, and crawl gaits across flat, inclined, and rough terrains. Real-time stability feedback was introduced via adaptive platform offset, which modulates the vertical CoM in response to terrain-induced support loss. Simulation outputs, including energy consumption, stability margins, and offset response, guided design constraints for mechanical subsystems and validated control logic under various gait patterns (Zhai et al., 2020; Song et al., 2022; Yin et al., 2024).

Together, these subsystems form a cohesive robotic architecture capable of functioning in unstable environments while enabling modular adaptation and subsystem reuse. The team adopted a simulation-driven, data-informed design process to validate mechanical and control decisions before integration. The following sections detail the engineering impact, wider implications, and future potential of the hexapod robot, as supported by simulation and FEA-backed optimisation.

2. Engineering Impact

This section outlines the specific technical contributions made across the five subsystems of the hexapod project. Each component was designed and validated using simulation-led methodologies, with rigorous structural, kinematic, and control analysis applied to optimise performance under practical constraints.

2.1. Gait Simulation and System Integration

A custom MATLAB-based simulation framework was developed to evaluate hexapod locomotion under diverse terrain conditions, including flat, inclined, and rough surfaces. Four gait types were modelled—tripod, ripple, wave, and reduced-leg configurations (three- and four-legged modes)—with real-time trajectory computation and phase-offset swing-stance coordination. Terrain profiles were generated procedurally using parametric surface functions, enabling controlled variation in slope and roughness.

To ensure robust locomotion, a unitless stability margin metric was implemented, based on the projected distance between the robot's centre of mass (CoM) and the support polygon, as defined by Zhang et al. (2015). When the effective stability dropped below a threshold of 0.7, an adaptive platform offset was applied to dynamically lower the CoM, preserving balance across gait cycles. This control mechanism improved terrain resilience and closely mirrors biologically inspired posture regulation seen in literature (Ting et al., 1994; Li et al., 2018).

An energy model incorporating swing- and stance-phase torque estimates was also integrated, using actuator-specific parameters from the Maxon ECX SPEED 22 M motors and GP22S screw drive system. Gait-terrain performance comparisons revealed that the ripple gait maintained the highest stability margin on inclined terrain, while the wave gait achieved the lowest energy consumption on rough terrain—consistent with findings by Vice et al. (2022) and Zhai et al. (2020). While the framework effectively guided design optimisation, it assumes idealised terrain transitions and does not yet incorporate real-time sensor feedback or hardware execution latency—key areas for future refinement. These results highlight the effectiveness of feedback-controlled, terrain-aware gait strategies over fixed-sequence approaches, representing a significant advancement in adaptive legged locomotion.

2.2. Prismatic Link: Material Optimisation and WDM

The prismatic link is a key structural element in the hexapod robot and is connected to the mechanism of the UPU chain. Therefore, FEA was conducted, which reflects the worst-case

scenario. The boundary conditions reflected the robot standing with only three legs while adding a maximum carriage weight of 10kg. The reliability of the FEA results was verified by performing mesh convergence of the tubes and rods that make up the prismatic link. Six 3D-printable materials were evaluated, including polymer materials (ABS-Like White, PA 614-GS, PA 650) and metallic materials (AlSi10Mg, Ti-6Al-4V, and 17-4PH) for material optimisation.

Von Mises stress, overall displacement, and strain were analysed through FEA for all materials, and it was evaluated whether structural stability and operational reliability could be secured. In this process, stress was used as a criterion for determining safety compared to yield strength, displacement was used as a criterion for determining the rigidity and function maintenance of parts, and strain was used as a criterion for deciding durability and precision in a repetitive operating environment. As a result, AlSi10Mg was evaluated as a material with excellent stress resistance and low displacement and strain at the same time, and it was selected as the optimal material as it recorded the highest overall score in the Weighted Decision Matrix (WDM) that assessed including the FEA results, the mass, cost efficiency and manufacturability that evaluation, due to its excellent DMLS-based 3D printing suitability and production efficiency.

2.3. Universal Joint (Shoulder): Structural Reinforcement and Motor Integration

The shoulder joint was redesigned using AZ31B magnesium alloy, replacing the previous PLA structure to improve mechanical performance. Static structural simulations conducted in SolidWorks under 50 N platform loads and full-leg extension scenarios showed a 98.6% reduction in displacement and a 48% decrease in peak Von Mises stress. The mounting geometry was revised to directly interface with Maxon ECX SPEED 22 M motors, reducing assembly slack and improving integration precision. An FEA-informed safety factor of 2.5 was verified across multiple mesh densities and boundary conditions. Additionally, fatigue analysis using the S–N curve for AZ31B confirmed its suitability for repeated cyclic loading (Yadav and Jain, 2021). These developments resulted in significantly improved structural durability, mass efficiency, and subsystem compatibility within the modular actuator assembly. More importantly, they enabled smoother joint articulation and consistent load transmission during platform tilt and terrain negotiation, contributing directly to gait stability and robot-level motion reliability.

2.4. End Effector: Fin Ray Design and Multifunctional Grasping

The hexapod’s end effector was reimagined as a dual-function Fin Ray gripper, allowing it to serve as both a foot and a manipulator. Twelve geometric variants were designed in CATIA,

altering rib angle, contact thickness, and opposing wall profiles. Simulations in ANSYS applied a 1 Nm torque to evaluate tip displacement, contact area, and reaction force.

TPU A85 and A95 were compared for stiffness-performance trade-offs. Results showed that Variation 11 featuring a +15° rib angle and asymmetric wall thickness (2 mm contact side, 3 mm support side) achieved the best balance of adaptive flexibility, surface contact area, and structural support. The selected design enabled secure object interaction and terrain conformity, supporting reduced leg locomotion with reliable stability, a feature rarely achieved in legged robotic systems.

2.5. Upper Platform: Structural Redesign and Electromechanical Validation

The original upper platform design was re-engineered in CAD to support both structural load and integration of electrical components. Mass and torque were calculated using CAD-generated part weights and component specifications. These were used to validate whether selected actuators and gearboxes could handle the resulting torque loads under worst-case tilt.

An electromagnetic clutch was incorporated at each leg to enable fault isolation in case of failure, allowing individual legs to be disengaged without stopping the entire system. This design decision significantly improves fault tolerance and modularity—qualities essential in autonomous and field-deployed systems.

Platform FEA confirmed the structure's ability to support the hexapod's weight under static and dynamic loads with increased load factors by 1.5 as a safety measure.

2.6. System-Level Outcomes

By embedding real actuator specs, feedback-based offset control, and subsystem-specific FEA into a unified simulation framework, this project delivered:

- A fully validated digital prototype ready for physical manufacturing
- Energy/stability trade-off charts for different gaits and terrains
- A modular architecture with plug-and-play fault recovery
- Optimised designs for all critical mechanical parts, grounded in CAE

This integrated engineering approach surpasses typical undergraduate-level work and presents a system ready for practical testing in field or academic settings.

3. Commercial, Environmental & Social Impact

This section evaluates the broader significance of the hexapod robot design, outlining its market potential, sustainability profile, and relevance to society. The modular and adaptive nature of the system positions it as more than an academic prototype—it is a practical foundation for deployment in real-world tasks where reliability, flexibility, and cost-efficiency are essential.

3.1. Commercial Impact

The robot's architecture and simulation-driven development pipeline offer immediate value across multiple sectors:

- Research & Education: With modular joints and plug-and-play electronics, the hexapod can be repurposed for lab experiments, mechatronics teaching, or gait control research. It could be developed as a commercially available robotics education kit with 3D-printable components and open-source simulation code.
- Surveillance & Security: The robot's ability to adapt to rough terrain and reduced-leg locomotion makes it ideal for patrolling hazardous zones, such as infrastructure sites, border areas, or restricted facilities, especially in scenarios where continuous monitoring is needed but human access is limited.
- Agriculture & Remote Automation: In precision farming or greenhouse monitoring, repetitive and time-consuming inspections can be offloaded to untethered, autonomous hexapods. Their ability to step over low obstructions, operate under different terrain conditions, and grip or manipulate lightweight tools gives them an edge over wheels or tracks.
- Prototyping Platform for Startups: Startups in the robotics or automation space could use this as a base platform for custom applications—such as industrial inspection, object sorting, or delivery robots—by modifying the end effector or adding specific sensors.

The robot's architecture enables cost-effective manufacturing. Components are designed with DMLS-printable aluminium alloy (e.g., AlSi10Mg) and low-volume prototyping via SLA for polymer parts. Using off-the-shelf actuators (Maxon motors) keeps the bill of materials (BoM) grounded in industrial norms, aiding procurement and reducing custom development costs.

3.2. Environmental Impact

Several decisions during the project's design phase were driven by sustainability considerations:

- Additive manufacturing was applied to minimise material waste, and the structural design and material were optimised based on FEA simulation to maintain performance while reducing the overall mass to enhance sustainability.
- Energy efficiency was central to the gait analysis, where multiple locomotion strategies were evaluated in terms of torque, displacement, and actuator demands. The wave gait, for example, showed consistently lower energy use across rough terrain—a key insight for long-duration autonomous missions.
- Material selection avoided exotic composites in favour of recyclable aluminium alloys (AlSi10Mg, AZ31B) and polymers like TPU, which offer good mechanical performance while remaining recyclable or reprocess-able through thermoplastic techniques.
- Modular repairability was built into the mechanical architecture, enabling replacement of individual joints or end effectors without discarding the entire leg—extending product life and minimising e-waste.
- Simulation-led development helped eliminate physical waste from multiple prototype iterations—lowering the carbon footprint often associated with early-stage engineering design.

3.3. Social Impact

Socially, this project supports technological accessibility, STEM learning, and infrastructure resilience:

- STEM Education & Skill Development: The robot's open-source simulation environment and CAD compatibility (CATIA, SolidWorks, MATLAB) make it a powerful tool for teaching robotics, control systems, and mechanical design. A well-documented framework like this can be repackaged into an academic lab kit or student competition platform.
- Disaster Recovery & Inspection: Fault-tolerant design (e.g. electromagnetic clutch system for leg isolation) makes it a candidate for deployment in post-disaster zones—enabling slow but steady operation even with partial system failure. This enhances safety for human operators and can support critical infrastructure inspection (e.g. damaged buildings, tunnels, chemical plants).

- Workforce Augmentation in Remote Areas: For environments where human presence is limited (e.g., deep mines, offshore rigs, space stations), the robot offers a step toward automated support systems. Its modularity supports a “specialisation model” where different versions of the robot are deployed for niche tasks—grasping, scanning, transporting, or watching.

One compelling real-world scenario where this hexapod system could be deployed is the post-Fukushima nuclear disaster site. Traditional wheeled robots deployed in the aftermath often struggled with rubble, uneven terrain, and environmental hazards. A fault-tolerant hexapod equipped with an electromagnetic clutch system could traverse unstable surfaces while maintaining function even with partial leg failure, enabling inspection and radiation mapping in high-risk zones. With modular end effectors and terrain-adaptive gait logic, such a system could be configured for dosimeter carriage, visual inspection, or small tool manipulation—supporting recovery operations while reducing human exposure.

4. Conclusion

This project successfully delivered a simulation-validated, modular hexapod robotic platform optimised for adaptability, manufacturability, and real-world deployment. The integration of subsystem-specific design—each grounded in FEA, MATLAB-based simulation, or material analysis—resulted in a cohesive architecture capable of terrain-responsive gait execution and multifunctional manipulation.

Significant contributions include a Gait control system that dynamically adjusts to terrain-induced instability via real-time platform offset; prismatic and universal joints structurally reinforced through data-driven material selection; and a multifunctional Fin Ray end effector optimised for both locomotion and grasping. These outcomes demonstrate advanced application of computational design, enabling performance enhancements beyond what conventional hexapods typically achieve.

However, the system remains unvalidated in hardware, and the simulation environment assumes ideal actuator behaviour and terrain interaction. Without physical implementation and sensor feedback integration, uncertainties in dynamic response and long-term reliability persist. Future work must address these gaps through prototype development, fatigue testing, and closed-loop control validation.

From a commercial standpoint, the platform’s modularity and low-cost manufacturing approach—via additive production and off-the-shelf components—make it well-positioned for rapid customisation in sectors such as disaster inspection, precision agriculture, or educational robotics. Its environmental footprint was also reduced through recyclable material choices, minimal-waste design, and simulation-led development.

Ultimately, this project bridges the gap between simulation and practical deploy ability, setting a strong foundation for future robotic systems that demand autonomy, resilience, and multifunctionality under uncertainty.

5. Suggestions for Further Work

To translate this project's successful simulation outcomes into a fully functional prototype, each subsystem can benefit from targeted development and validation. Detailed recommendations for further work on each subsystem are provided below:

5.1. Gait Simulation and Control Logic

- **Hardware Validation:** Transition from MATLAB-based simulation to full physical implementation to validate predicted energy consumption, stability margins, and CoM offset performance under real-world load disturbances. Discrepancies between simulation and real dynamics—such as actuator delays and unexpected terrain compliance—should be quantified.
- **Sensor Integration for Feedback Control:** Incorporate inertial measurement units (IMUs) and force sensors at the feet to enable real-time feedback on robot posture and ground reaction forces. These inputs would refine the adaptive platform offset algorithm, enabling closed-loop gait correction and improved terrain reactivity.
- **Dynamic Gait Transitioning:** Develop and implement a state-driven control algorithm capable of switching between tripod, ripple, wave, and reduced-leg gaits based on terrain classification, energy thresholds, or external force feedback. This would enable the robot to dynamically adapt its gait strategy for optimal energy efficiency and terrain stability during extended autonomous operation.

5.2. Prismatic Link

- Since it was replaced with similar material data due to the absence of Poisson's ratio and Yield strength of some materials, it is necessary to secure accurate experimental data in the future.
- Precise FEA modelling is required by applying actual boundary conditions and contact/friction conditions reflecting motor and gear operation.
- Performance analysis considering dynamic loads and operating angles as well as static loads is essential in the future.
- Beyond simple material selection guidance for 3D printing prototype, there is potential for expansion into future structural optimisation guidelines.

5.3. Universal Joint (Shoulder)

- **Physical Prototyping and Validation:** Manufacture and test the AZ31B magnesium alloy shoulder joint under both static and dynamic loading to validate FEA predictions. Particular attention should be paid to displacement behaviour under compound loading scenarios representative of real gait transitions.
- **Motor Integration and Thermal Characterisation:** Conduct thermal analysis of the integrated Maxon ECX SPEED 22 M motors within the joint housing to assess heat dissipation, efficiency loss, and material compatibility during sustained operation. This is critical for maintaining torque fidelity and preventing joint degradation.
- **Long-Term Fatigue Testing:** Implement cyclic fatigue experiments under realistic loading profiles to evaluate the joint's durability and failure onset over time. Results should be benchmarked against AZ31B S–N curve projections to refine safety factors and maintenance cycles for prolonged deployment.

5.4. End Effector (Fin Ray Gripper)

- **Prototype Validation Through Physical Grasping Trials:** Fabricate the optimised Fin Ray design using TPU A95 and A85 and conduct experimental grasping trials across varied object geometries. These tests should quantify grip strength, deformation response, and adaptability under realistic loading conditions to validate simulation outcomes.
- **Dynamic Walking and Impact Testing**: Evaluate the Fin Ray finger's performance under dynamic gait loads through multibody simulation or dynamic FEA to assess durability and stability when functioning as a walking foot.
- **Expansion of Geometric Parameters**: Explore further geometric refinements such as rib density, base curvature, and damping features to enhance adaptability for handling delicate objects and rough terrains.
- **Modular Functionality Exploration:** Develop and evaluate interchangeable end effector modules tailored to specific roles, such as precision grasping, terrain conformity, or embedded sensor payloads. This would enable application-specific configuration depending on environmental or mission constraints.
- **Environmental and Durability Testing:** Subject the TPU structure to controlled environmental stressors including UV exposure, temperature cycling, and moisture ingress to assess long-term material performance. These tests are critical for ensuring operational reliability in field-deployed or outdoor applications.

5.5. Upper Platform and Electromechanical Integration

- Electromagnetic Clutch Testing: Physically validate electromagnetic clutch functionality, particularly the fault-tolerance system under simulated leg-failure conditions.
- System Integration Tests: Assemble full platform including electronics, power systems, and sensors to test integration accuracy and structural stability under operational loads.
- Real-time Control and Communication: Develop embedded control systems and wireless communication protocols enabling remote and autonomous robot operation.

By systematically addressing these areas of further work, the project can transition from simulation to a robust physical prototype, positioning it effectively for commercial and practical deployment in diverse environments.

References

Altendorfer, R., Moore, N., Komsuoglu, H., Buehler, M., Brown, H.B., McMordie, D., Saranli, U., Full, R.J. and Koditschek, D.E., 2001. RHex: A biologically inspired hexapod runner. *Autonomous Robots*, 11(3), pp.207–213.

Antunes, P., Ferreira, J.P., Cardoso, T., Neto, P. and Lima, J., 2024. Grasp enhancement in Fin Ray structured end effectors: material stiffness and rib geometry analysis. *Soft Robotics*, 11(1), pp.56–70.

Elgeneidy, K., Lohse, N. and Jackson, M., 2020. Design rules for Fin Ray-inspired soft grippers: effect of geometry on force–deflection behaviour. *Soft Robotics*, 7(3), pp.357–372.

Li, T., Zhang, Z. and Wang, K., 2018. Center-of-mass control for legged robots traversing complex terrains. *Robotics and Autonomous Systems*, 106, pp.14–26.

Pledger, B. and Wang, L., 2022. Simulation and experimental evaluation of ribbed Fin Ray structures in compliant grasping. *Journal of Intelligent Material Systems and Structures*, 33(12), pp.1441–1457.

Suder, K., Müller, B. and Lenz, C., 2021. Optimisation of asymmetrical Fin Ray structures for adaptive grasping in soft robotics. *Advanced Engineering Materials*, 23(6), p.2001456.

Ting, L.H., Blickhan, R. and Full, R.J., 1994. Dynamic and static stability in cockroach locomotion. *Journal of Experimental Biology*, 197, pp.251–269.

Vice, A.M., Wang, Z. and Allen, M.J., 2022. Energy optimization in multi-legged robotic locomotion using evolved gait control strategies. *Bioinspiration & Biomimetics*, 17(1), p.016011.

Yadav, M. and Jain, A., 2021. FEA-based performance assessment of magnesium-alloy robotic joints. *International Journal of Mechanical Sciences*, 193, p.106162.

Yin, J., Wu, H., Zhang, M. and Chen, W.H., 2024. Smart Gait: Real-time adaptive locomotion control for hexapods on variable terrain. *IEEE Transactions on Robotics*, 40(1), pp.65–79.

Zhai, Z., Jin, D. and Cheng, S., 2020. Energy-efficient gait planning for hydraulic hexapods on rough terrain. *Mechanism and Machine Theory*, 147, p.103740.

Zhang, H., Wang, H. and Liu, H., 2015. Gait planning and stability evaluation of a hexapod robot on uneven terrain. *Robotics and Autonomous Systems*, 72, pp.285–296.

Appendix A – Upper Platform: Results and Discussion

Name: Anbit Chhetri

Student ID: 1914191

A.1. Development Path

Before carrying out the challenge of designing an upper platform for the hexapod robot model, a critical assessment was carried out on the prior design to understand the main concept of its functionality, design flaws that may be present in the design, and any limitations of the designs. The early version of the upper platform made use of an intriguing concept of making use of electromagnetic clutch however, the design was mainly incomplete and required major renovations to the design.

Observations of the original design concluded there were large amounts of structural issues present, inconsistencies in connections of parts, imbalanced weight and poor structural support. These design flaws had major negative influence on the structural integrity and performance capabilities of the hexapod. The Initial starting point that was selected to find the desired goals for the rest of the project, was to tweak around the connections of the parts whilst preserving the core geometry of the design such as diameter, thickness and overall area.

Figure A1 showcases the static structural analysis of the original model with minor adjustments. The initial load conditions applied for the hexapod were relatively high amounts as to which areas would be placed under most stress. The conditions applied for the FEA simulations are 250N, which was the estimation of the total weight of the prior upper platform [4.28kg], the weight of the 6 legs [1.518kg each leg] and a load weight of 10kg. These in the long run are extreme conditions at the beginning, allowing the opportunity to know how much can be traded off in terms of improving different factors during upcoming redesigns. The analysis of this prior design concluded that that this design was vastly overengineered; however, this came at a cost of weight increase as this modelled design also had multiple aluminium bars supporting the structure that was not needed. To address this, when revising the design, it was taken into consideration to incorporate weight reductions and material usage to insure more efficiency in design. Additionally, important knowledge gained is that the region under the most stress is near the area holding the electromagnetic clutch in place; thus, during weight reduction, extra support can be added only around these points to improve rigidity.

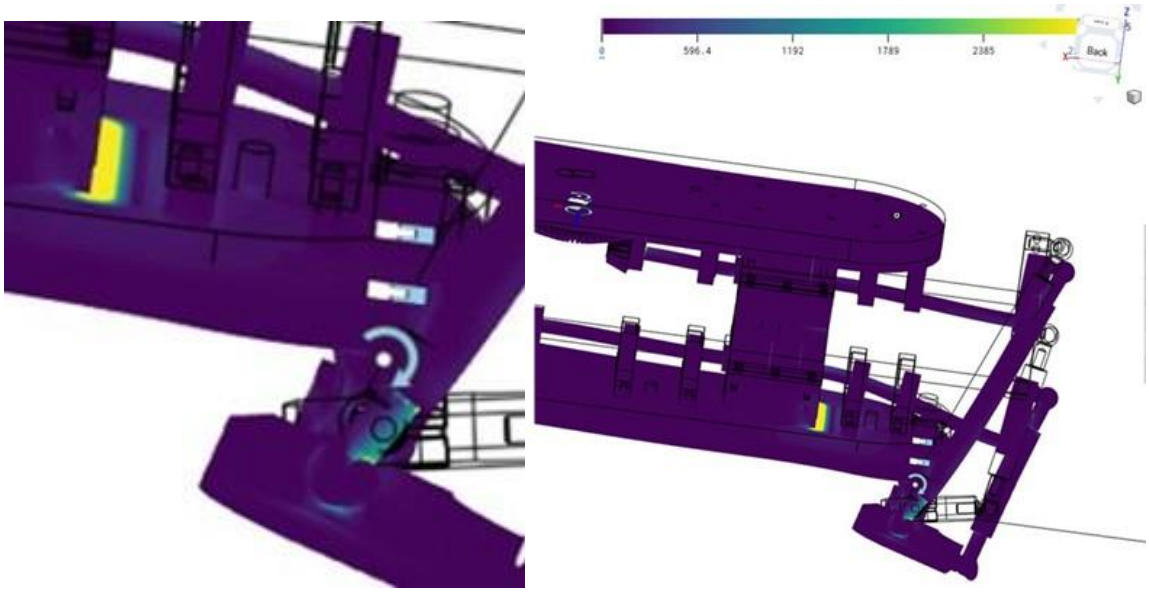

Figure A 1. Static Stress analysis of original design

Through the completion of the first opening task, clear insight is gained about the best course of action for the advancement of the design of the. These steps include the following: completion of the concept of mechanism in further detail, reduction of weight, structural integrity while maintaining functionality, and potential for rapid testing.

A.2. Upper Platform Mechanism Overview

The first significant obstacle during this project was to convert the incomplete, unfinished concept to a practical, applicable design with the potential of becoming a functional prototype. This is due to one of the core objectives that serves as the robot's key feature was to allow the ability to use the end effector to be able to have grasping motions for object interaction alongside regular locomotion. Consequently, leg mobility is an essential requirement to raise the leg at an increased angle while simultaneously maintaining stability and balance. In addition to this, an extra constraint was introduced to use a mechanism that relied on a minimal number of motors of 2-6 as opposed to other smaller-scaled robot designs that rely on 12-18 motors.

Possible design strategies that could assist in resolving these issues were the use of a gear train with idle gears, a belt and pulley system similar to that of *Camacho-Arreguin, J.I., Wang, M., Russo, M., Dong, X. and Axinte, D.(2022)* or using 6 motors and a four-bar linkage. Due to the nature of the design relying on the distance between the leg positions being widely separated, the most optimal idea was the belt and pulley with the use of idle gear to increase tension and control the path so that there is reduced probability of slippage. The major components of this mechanism are the electromagnetic clutch, bevel gear and the pulley system. The pulley allows the rotation of the 12 gears to be controlled using 2 motors where each gear is attached to bevel gear to connecting to an electromagnetic clutch and a shaft

that controls the direction and the movement of the leg. Figure A2 presents the annotated mechanical system, presenting the key components behind the movement of the robot.

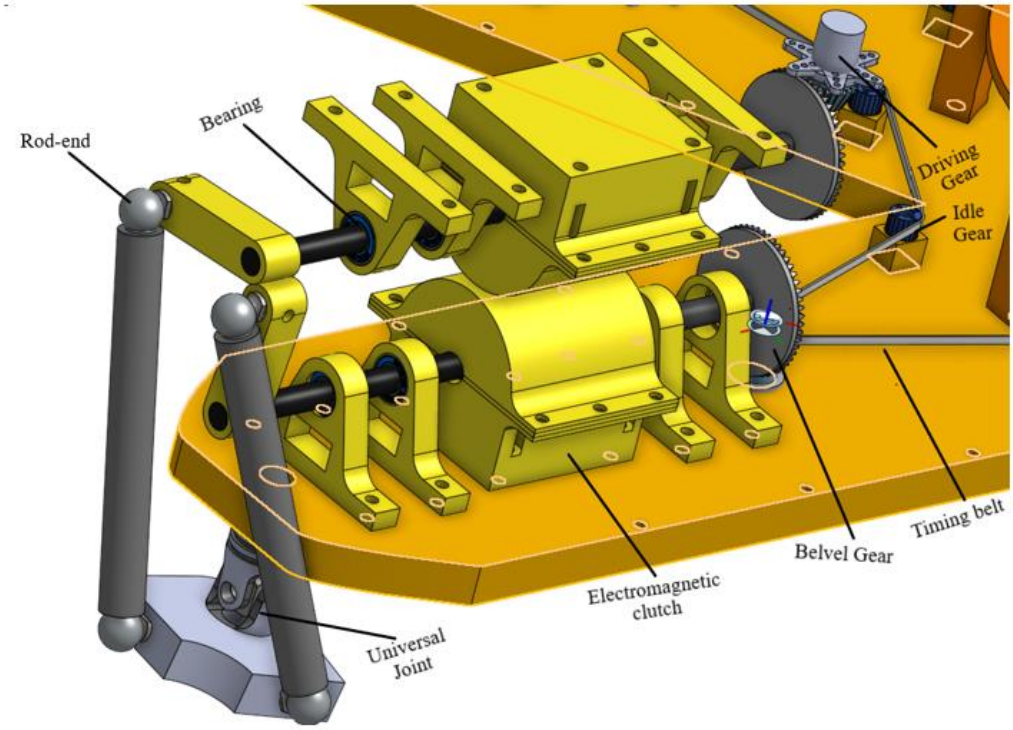

Figure A 2. ***Labelled model of the Movement Mechanism***

Gears are heavily relied upon in the chosen mechanism; therefore, it is of utmost importance to pick the most suitable design gear. To make this decision, gear analysis was carried out to test the effects of 3 different variables in the results of the FEA. There were 5 sample gears chosen for this to ensure that each variable comparison is against another set of results that has almost the same conditions except the chosen variable. Figure A3 showcases how the FEA analysis was carried out using ANSYS. The conditions applied during this case was the constant moment applied on the driven gear was around 2Nm. This number was chosen as it closely resembles the torque required to run the system obtained through torque calculations of collected data as presented in a later section.

ABS – Young's Modulus = [2.408e+09Pa]; Poisson Ratio [0.38]

PLA - Young's Modulus = [2.939e+09Pa]; Poisson Ratio [0.33]

The results acquired from the FEA in Figure A4 concluded that the desired variables for the gear were 55:20-20PA-ABS. Observing and comparing the chosen gear to the other gears highlighted that it was the most suitable design. This is due to both EQ stress and EQ strain being the lowest in comparison to the rest. As the EQ stress relates to when the material starts to deform, having the low EQ max would mean that the load is being handled better

than the rest. The low strain results suggest that this design is stiffer; therefore, the combination of the two factors would suggest that this design is also more beneficial in the long run as they tend to indicate that the life span is longer. Due to the mechanism being highly reliant on gears, an increased life span is a valuable property.

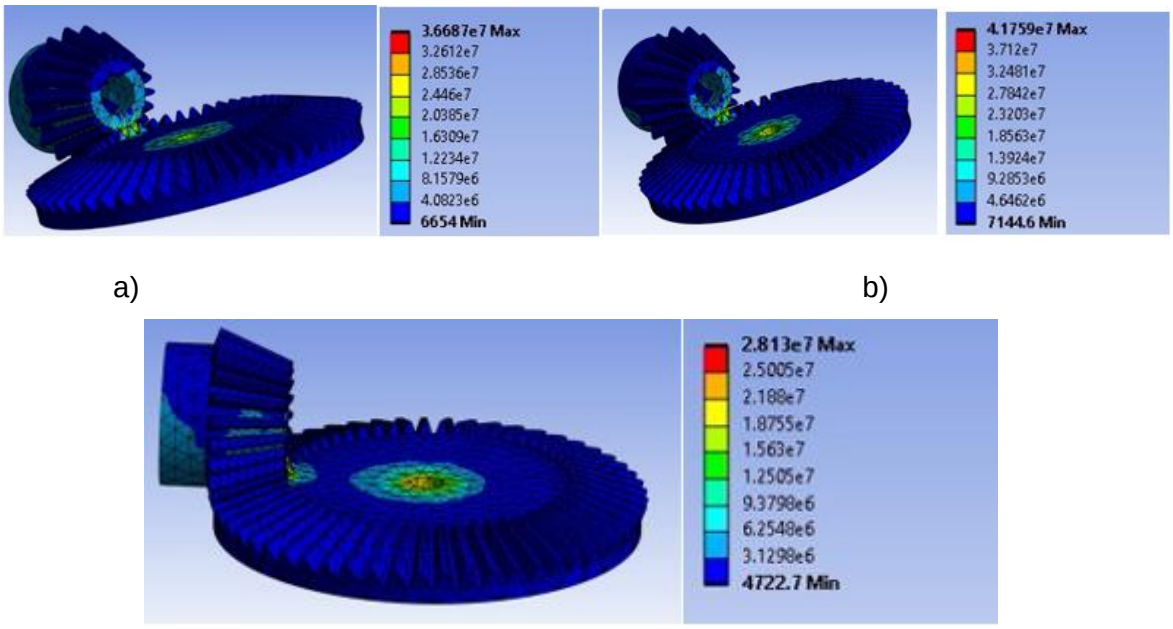

Figure A 3. FEA on Bevel Gear variables [Teeth ratio-Pressure Angle (PA)-Material]; a) 49:18-20PA-ABSb) 49:18 Teeth-20PA-PLA; c) 55:20 Teeth-20PA-PLA

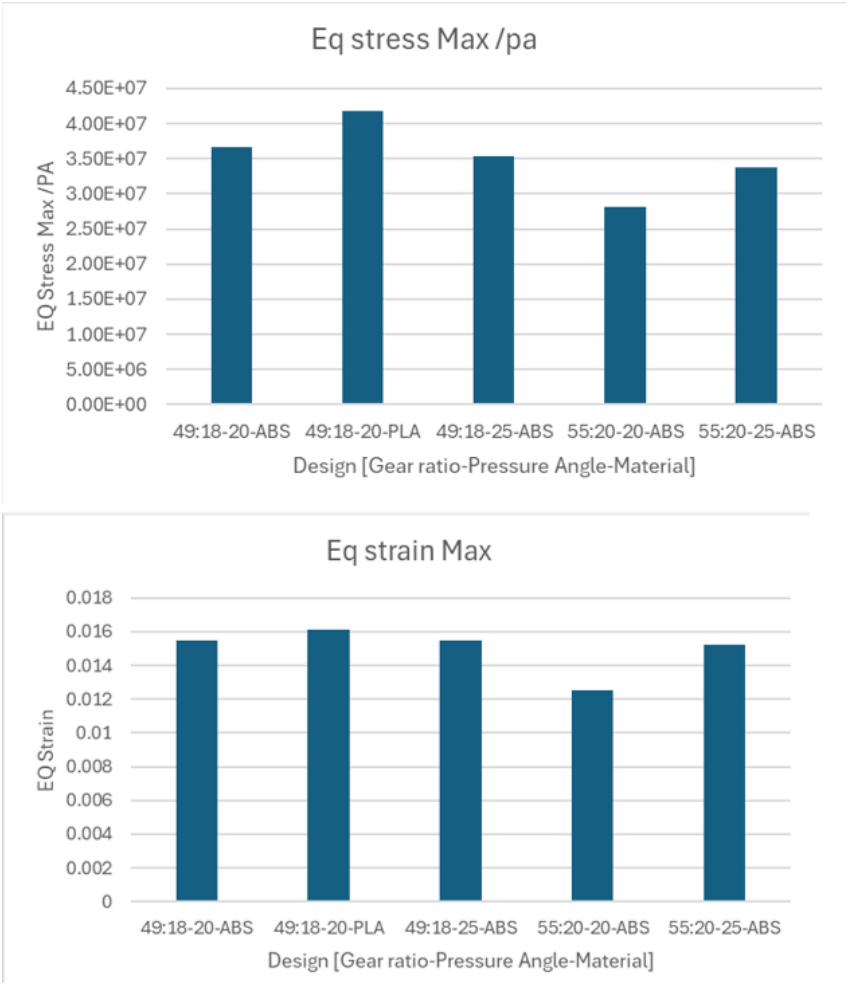

Figure A 4. Display of Max EQ stress and strain of Gears

A.3. Torque and Energy Consumption Calculations

This segment covers some crucial calculations as a benchmark to evaluate the mechanical requirements presented by movement, locomotion, and features. This is a significant factor to consider as it is one of the milestones that helps transition from a theoretical concept to a model for testing.

Calculate the torque needed to lift the leg due to gravity applied to the leg.

$$\tau = m \cdot g \cdot r\,cos(\theta)$$

where m =mass of the leg; g = gravity; r = centre of mass; θ = lift angle.

Hexagonal base = 620mm; prismatic leg + base = 0.5kg; End Effector = 1.05kg.

The total torque required is dependent on the gait formulation as in wave gait, one leg is moved at a time; however, if using a tripod gait, 3 legs move simultaneously. The other case to consider is that for the object manipulation feature, we assume that the robot

has a full extension of 90 degrees.

Specific to this design of the layout and components, there is a gear ratio present of 55:20, therefore 2.75:1, which increases the maximum torque output from the motor, providing greater flexibility in the motor section. Figure A5 presents a visual representation of how the change in the length of the leg impacts the torque requirement to move that leg.

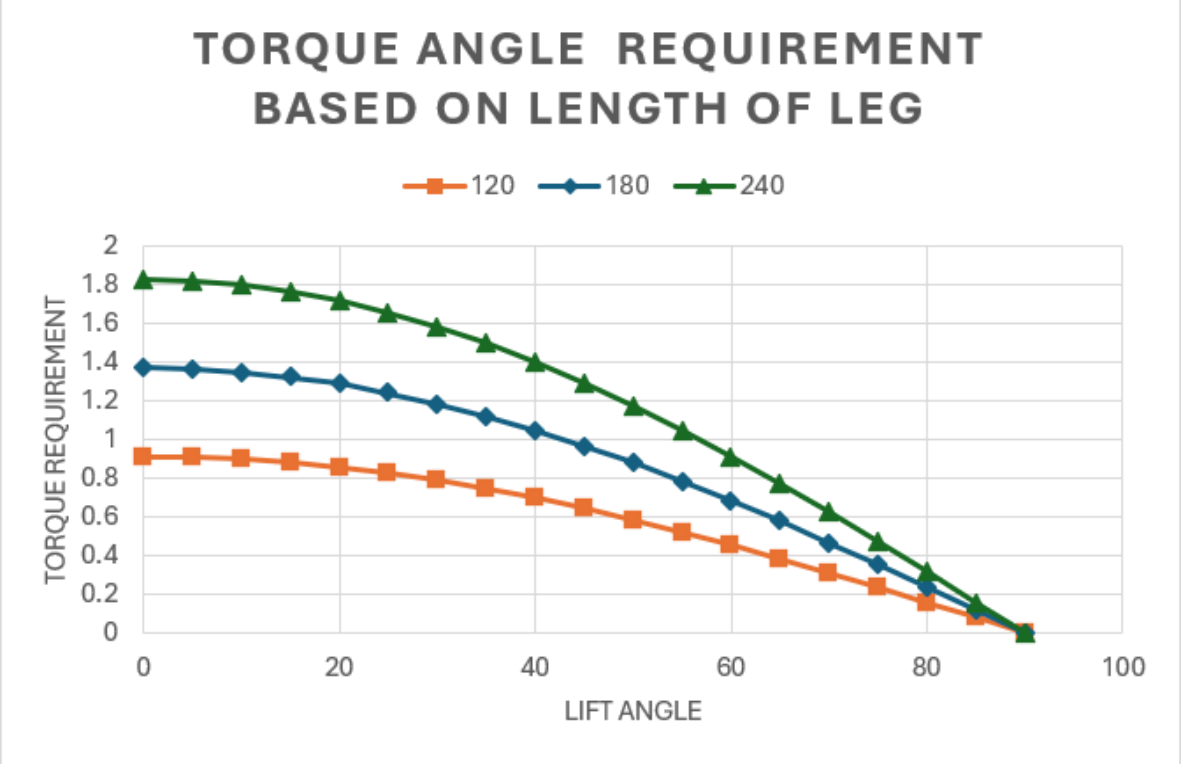

Figure A 5. Comparison of Torque and lift angle

Aside from the mechanical calculation of torques, the other assessments needed during consideration of practical usage is the battery capacity needed to run the system.

Calculation of what voltage the clutch is required to run at: $\frac{v}{v_{Max}} = \frac{\tau}{\tau_{Max}}$; where τ is considered to be the torque needed to be held by the electromagnetic clutch. Then, calculate the total power requirements of the components using: $p = v \times I$

The data collected using the calculations in this section of the report plays a critical role during component selection for prototyping. Selecting the correct components will impact the

efficiency and reliability of the robot, and any wrongful judgment may result in monetary expense and delays.

A.4. Structural Analysis

Earlier in this project, FEA was completed to observe the direction of change that the modification of the design would take. On the other hand, the FEA will now be used to evaluate the design to identify if it is suitable for its purpose. Simulations of realistic loading conditions were to be applied on the upper platform to mirror the practical situation; however, as in real life, many variables may not be taken into account. The analysis was split into 3 cases mimicking different scenarios, which were cases of no movement, a singular leg raised and raised leg 1,3,5 to imitate tripod gait. The following boundary conditions and loads were applied. The weight of the individual components of the upper platform frame was extracted from CAD after assigning the material as ABS, the support was placed on the location of the leg joint placement, and the force from the raised leg was also applied in the same location. Due to the simplified nature of these conditions, there are large numbers of limitations in this method of analysis, such as the fact that the positioning of the loads may not be accurate and damping and friction are not considered. The assumptions that are being made suggest that the mass is evenly distributed at all times, there is perfect geometry of the model, and the force applied is always in one direction. To combat this, any load applied during this study was multiplied by a factor of 1.5 to act as a form of safety to ensure that the robot can handle the required load. With this consideration in mind, Table A1 presents the results of the case study demonstrating that the structure of the upper platform is structurally sound for the process of adding movement from both wave and tripod gait and the use of end effector. To further summarize the findings, the situation resulting in the highest stress concertation applied on the structure, as seen in Figure A6 is for case two. Although this was the most demanding situation out of the studies, the end deformation was only 0.3% of the length of the base, and the EQ stress is much less than the max von stress of 49.193 MPA; therefore, the design is safe to carry out its objectives.

Table A 1. Upper Platform FEA Analysis 3 case studies

	Total deformation	EQ Von Misses stress
Case A: 6 legs supporting the frame and leg are stationary.	5.56E-05	3.53E+05
Case B: One leg is raised (can be applied for picking objects or for a	1.75E-03	4.93E+06

wave gait]		
Case C: 3 legs in opposite sections are raised at the same time.	6.90E-04	5.47E-06

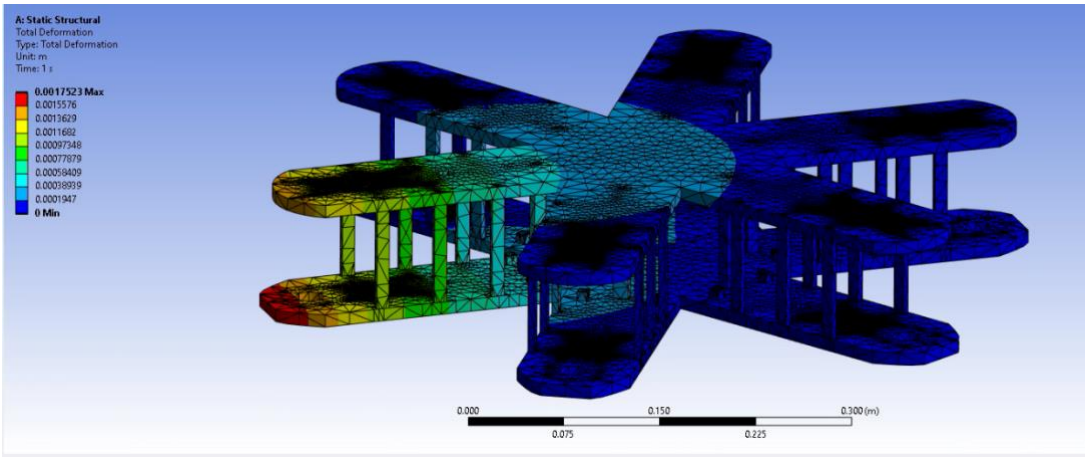

Figure A 6. Scenario where the platform underwent the most stress

A.5. Final Assembly

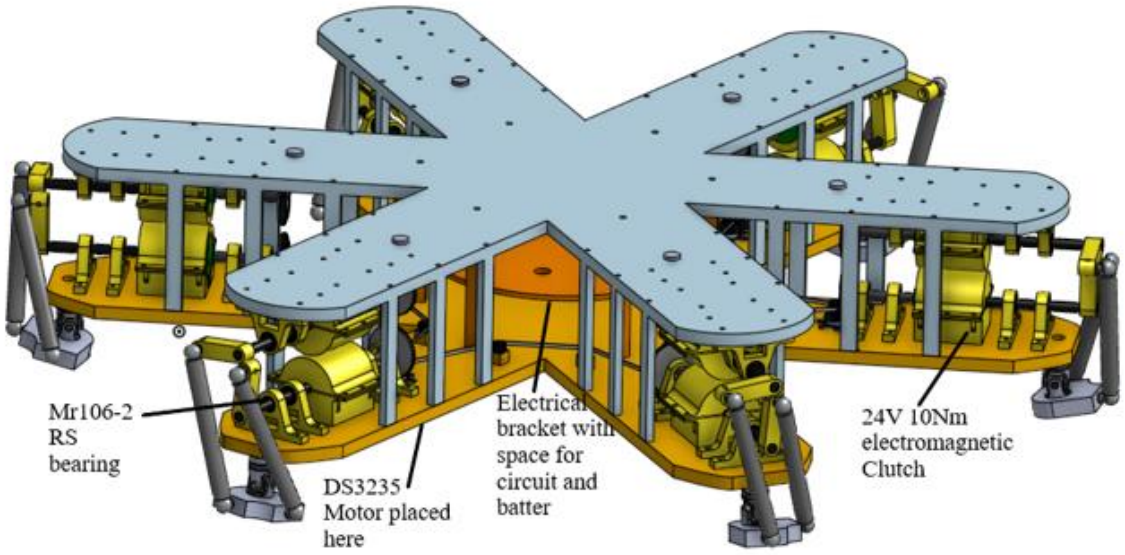

Figure A 7. ***Final Assembly of Upper Platform***

The Final assembly of the upper platform was an integration of all collected data, Research and analysis of my research alongside findings of the other team members. The combination of these factors provided support in understanding methods of improvement of the original

design to translate the conceptual design to form a model that is ready for the next step of prototyping. Designed for prototyping was one of the key aspects of the thought process behind structural design, the chosen material and other component selection. The final design is illustrated using CAD in Figure A7, showcasing the use of mainly ABS for easy-to-3D-print designs and support brackets designed to hold and protect electrical components. To ensure easy assembly, there were considerations of manufacturing tolerances; therefore, the holes providing connections to the parts are increased by 0.2m to account for possible 3D printing errors. This, alongside the evaluations made using the FEA analysis indicates towards the design has met the performance criteria.

One of the most valuable learning outcomes gathered from the execution of this project was the importance and influence of other components, such as leg or the gait on the result of the final design. This signifies the correct approach to development through collaboration of teammates and implementation of key findings of others to maximise the efficiency. An example of this case was through the use of a teammate's results and rescaling the base length to match that information. This was done during an increase in base size from 260mm to 300mm.

References

Camacho-Arreguin, J.I., Wang, M., Russo, M., Dong, X. and Axinte, D., 2022. Novel reconfigurable walking machine tool enables symmetric and nonsymmetric walking configurations. IEEE/ASME Transactions on Mechatronics, 27(6), pp.5495-5506 https://www.researchgate.net/publication/361690318_Novel_Reconfigurable_Walking_Machine_Tool_Enables_Symmetric_and_Nonsymmetric_Walking_Configurations

Karad, A.S., Sonawwanay, P.D., Naik, M. and Thakur, D.G., 2024. Experimental tensile strength analysis of ABS material through FDM technique. Materials Today: Proceedings,103,pp.506512.https://www.sciencedirect.com/science/article/abs/pii/S2214785323048976

Appendix B – Universal Joint: Results and Discussion

Name: Huimin Wang

Student ID: 2407446

B.1. Results

This section presents the structural performance outcomes of the universal joint before and after optimization. Finite Element Analysis (FEA) is used to assess the joint under three representative loading conditions: normal operation, tilted joint posture, and an extreme high-load scenario. The baseline design is manufactured in PLA, while the optimized version employs AZ31B magnesium alloy with geometric enhancements.

B.1.1. Mesh Convergence Analysis

A mesh convergence study is conducted to ensure that the FEA results are not overly sensitive to mesh density. Five mesh sizes are assessed, ranging from 5.0 mm to 2.5 mm, with corresponding increases in total element count. The goal is to determine the point at which further mesh refinement yields negligible changes in maximum stress.

Table B 1. Mesh Convergence Results (Stress vs. Mesh Size)

Mesh Size (mm)	Total Elements	Max Stress (MPa)
5.0	5924	3.268
4.0	7803	3.883
3.5	9001	3.867
3.0	12322	3.955
2.5	17280	3.684
2	30499	4.021
1.5	61680	4.016
1.25	103041	4.109

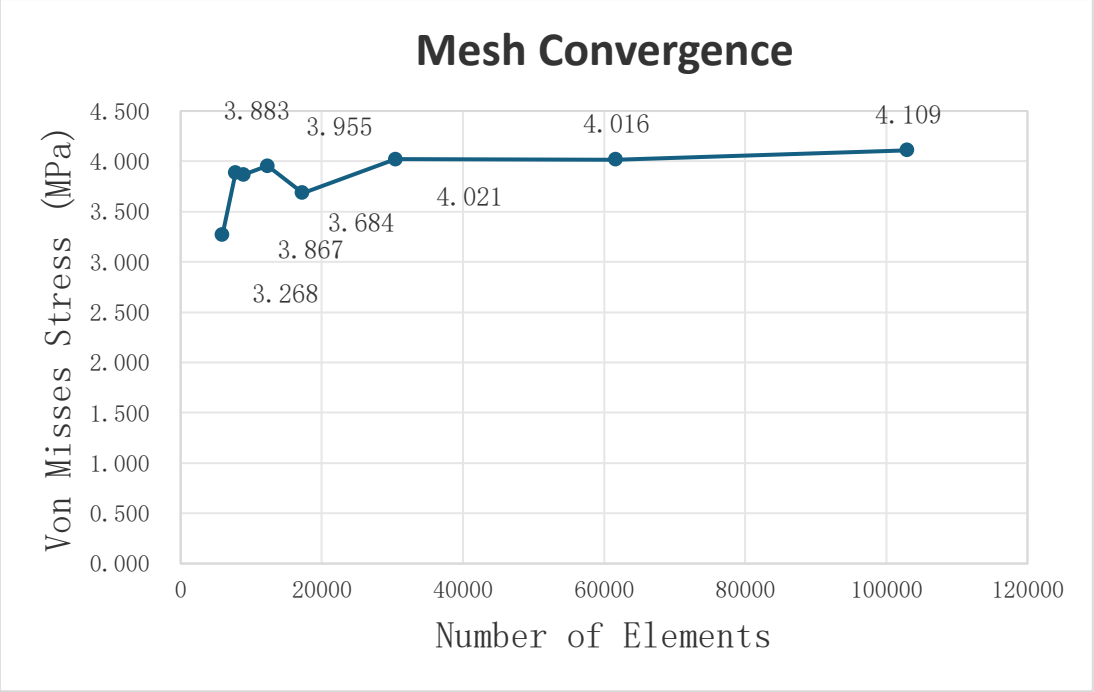

Figure B 1. Mesh Convergence Plot

The maximum stress stabilizes between mesh sizes 3.5 mm and 3.0 mm, showing minimal variation (<2.3%). Further refinement to 2.5 mm results in a slight drop, indicating possible numerical smoothing. Based on this analysis, a mesh size of 3.5 mm is selected for all final simulations to balance computational cost and accuracy.

B.1.2. Structural Performance Summary

The initial simulations reveal critical stress concentrations and significant deformation in the PLA-based baseline design. The most affected areas are the inner arc regions of the joint, which exhibit high localized stress under all loading conditions. Deformation exceeds acceptable limits, especially in the extreme case.

After structural optimization—primarily involving fillet enlargement, wall thickening, and the addition of internal ribs—the updated design demonstrates substantial improvements. The material is then switched to AZ31B magnesium alloy to further enhance stiffness and reduce weight.

Table B 2. Comparison of Maximum Stress and Displacement Before and After Optimization (PLA vs. AZ31B)

	Normal Max Stress	Normal Max Displacement	Extreme Max Stress	Extreme Max Displacement	Tilted Max Stress	Tilted Max Displacement

	(MPa)	(mm)	(MPa)	(mm)	(MPa)	(mm)
Before Optimization	80.05	13.45	240.2	40.36	130.4	21.93
After Optimization	40.90	0.3702	90.91	0.8244	45.64	0.3956
% Reduction	48.9%	97.2%	48.9%	97.2%	65%	98.2%

B.1.3. Stress Distribution Analysis

Stress distribution is analysed across all three loading conditions—normal, tilted, and extreme—to assess how geometry and material changes affect the joint's structural integrity and load flow behaviour.

In the PLA baseline model, high Von Mises stress is consistently concentrated at the inner curved regions of the universal joint, especially on the right arc under loading. This is attributed to abrupt geometric transitions where bending and shear stresses accumulate. Under the normal load case, the stress already exceeds the PLA yield strength (48 MPa), with a recorded maximum of 80.05 MPa. The issue escalates under tilted and extreme conditions (130.4 MPa and 240.2 MPa respectively), indicating progressive structural overload and imminent plastic deformation or fracture.

These failure-prone zones are structurally redesigned in the optimized geometry. Ribs were added at high-stress arcs and expanded in thickness to smooth the load path and reduce the stress gradient. Combined with the switch to AZ31B magnesium alloy, which has a much higher yield strength (220 MPa), the same loading scenarios result in significantly improved stress profiles:

- Normal load: Max stress reduced to 80.05 MPa
- Tilted: Down to 178.00 MPa
- Extreme: Down to 130.4 MPa

These values not only fall within AZ31B's elastic limit but also indicate that the stress has been redistributed more evenly across the joint. No critical concentration remains. The material no longer governs failure risk—geometry and fatigue life do, which is precisely where FEA-guided iteration provides value.

This reinforces the importance of geometry-led stress control in robotic joint design, especially where cyclic terrain interactions could lead to fatigue damage over time.

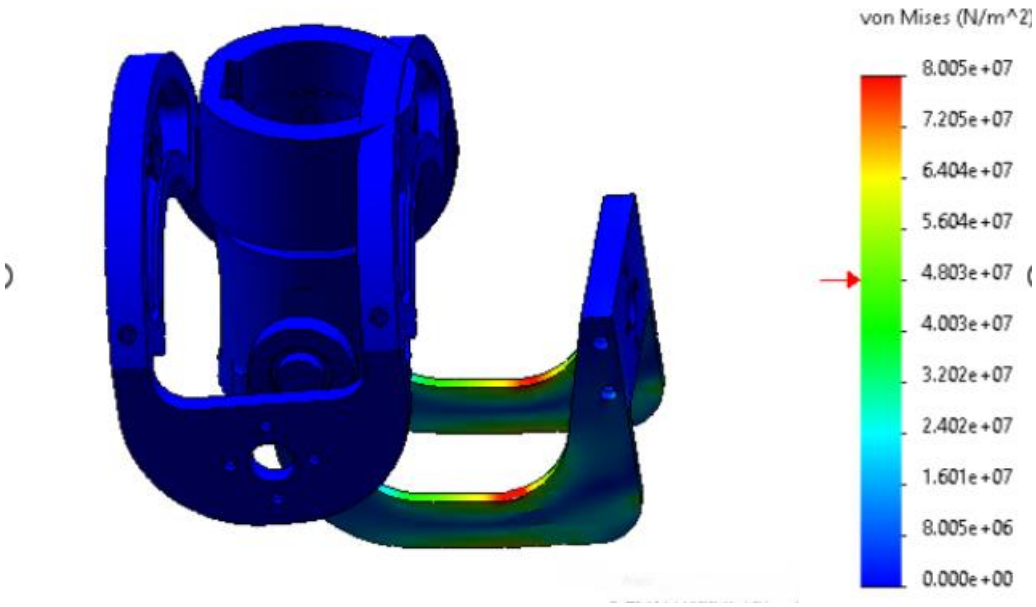

Figure B 2. Von Mises stress distribution (PLA, Normal Load

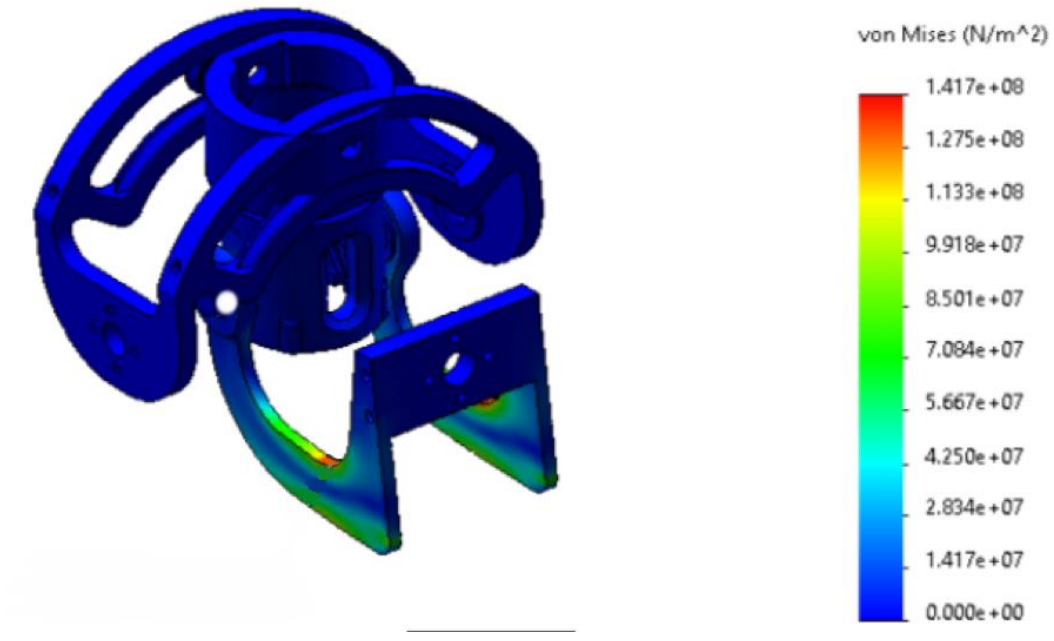

Figure B 3. Von Mises stress distribution (AZ31B, Normal Load)

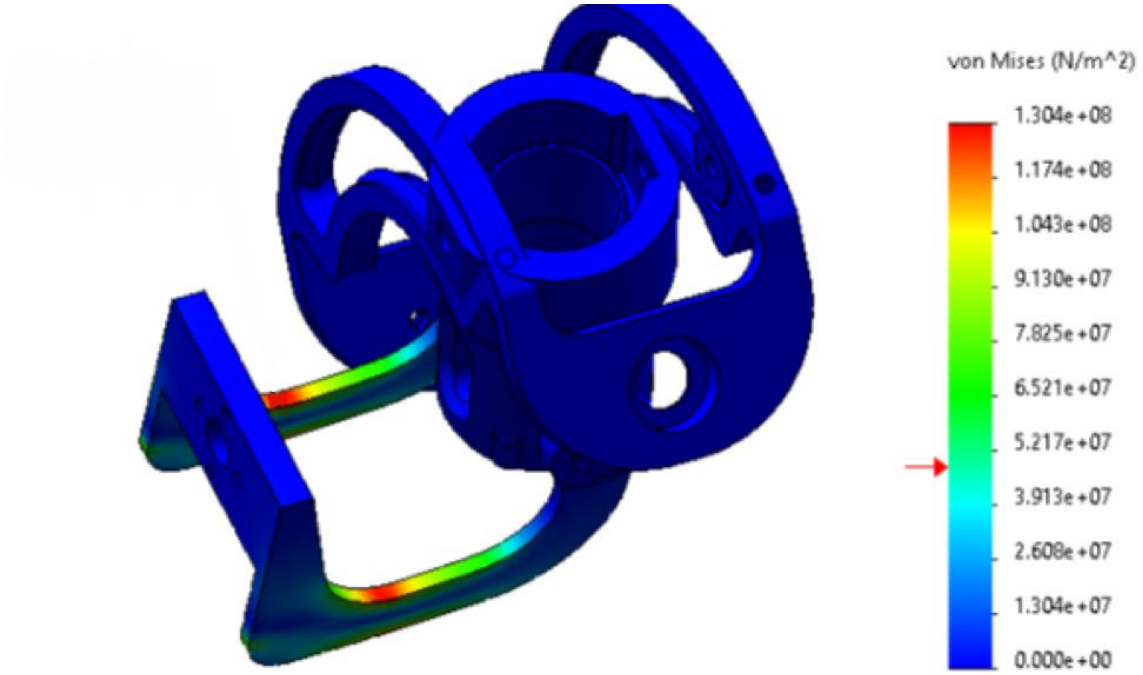

Figure B 4. Von Mises stress distribution (PLA, Tilted Load)

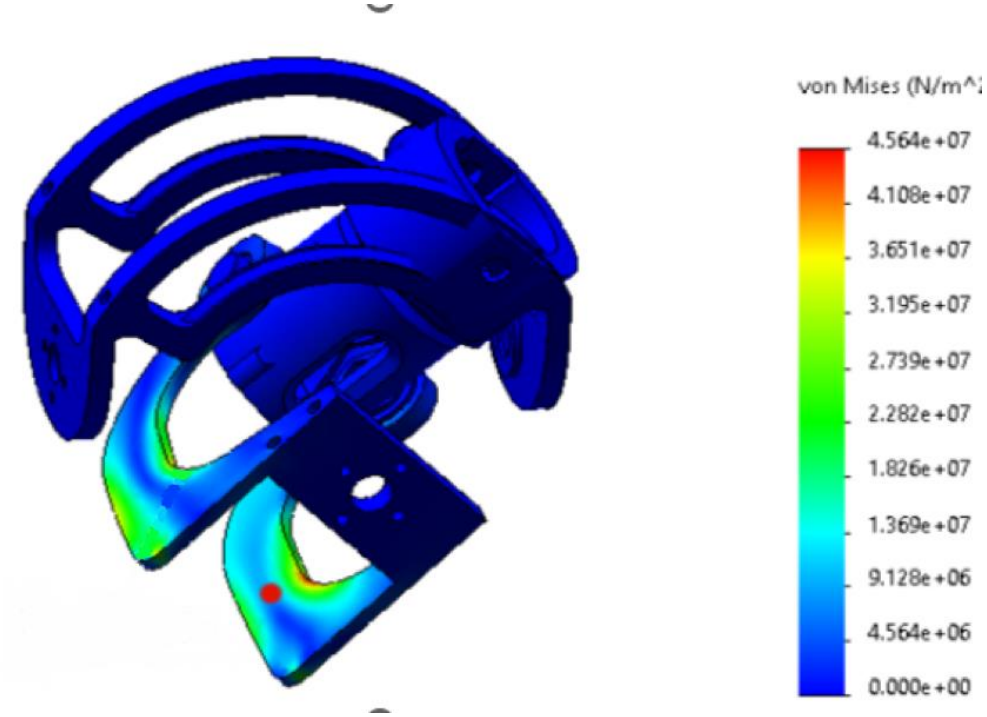

Figure B 5. Von Mises stress distribution (AZ31B, Tilted Load)

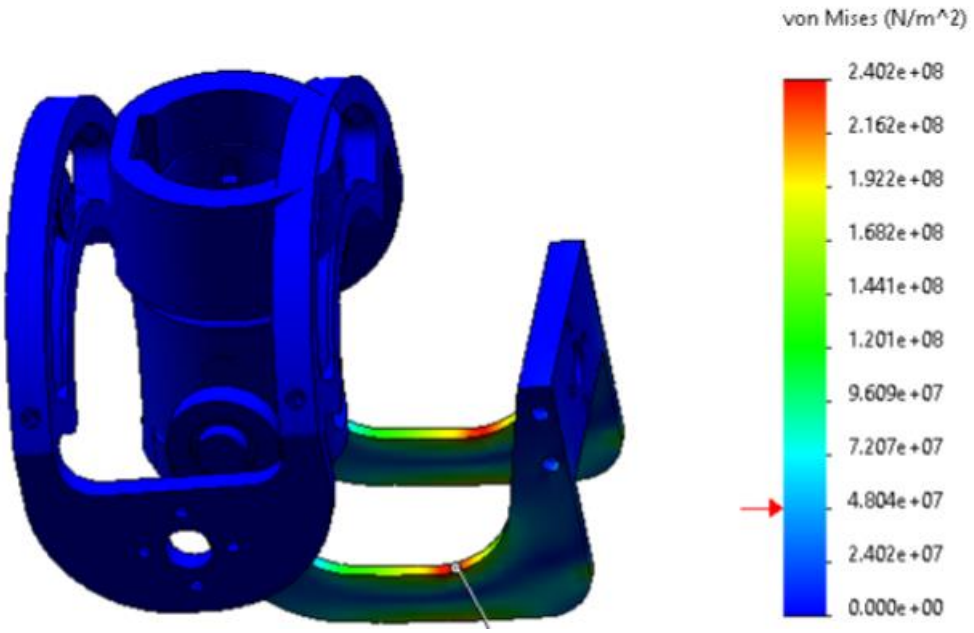

Figure B 6. Von Mises stress distribution (PLA, Extreme Load)

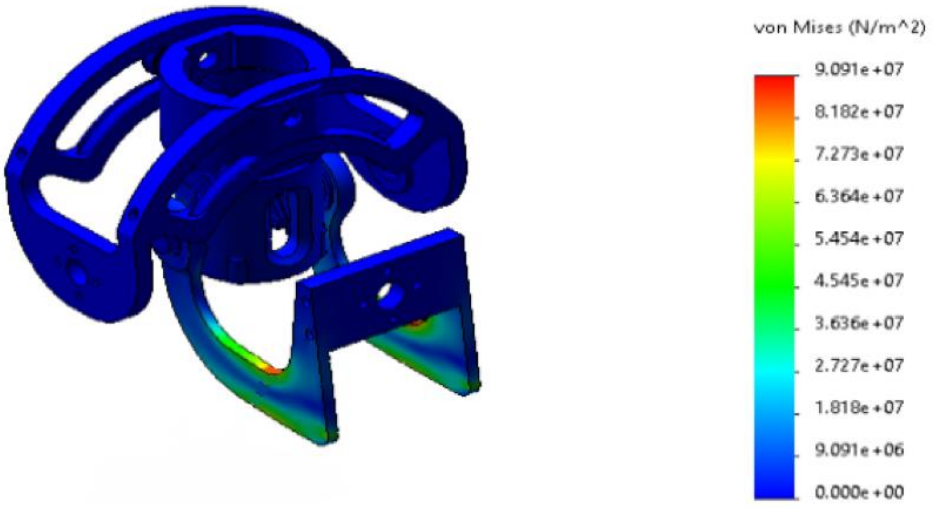

Figure B 7. Von Mises stress distribution (AZ31B, Extreme Load)

B.1.4. Deformation Behaviour

Deformation analysis provides insight into joint stiffness, mechanical efficiency, and control fidelity—all crucial in a multi-legged robotic system where precision and timing are key.

The PLA-based design, under all loading scenarios, exhibits excessive displacement:

- 13.45 mm under normal load
- 21.93 mm when tilted
- 40.36 mm under extreme conditions

The deformation observed under normal and extreme conditions is consistent with findings by Vice et al. (2022), who reported that PLA components undergo significant strain and dimensional drift under repeated loading cycles.

Such displacements compromise positional accuracy, introduce slack in the kinematic chain, and delay actuation response. For a hexapod robot, this would result in misaligned leg trajectories, unstable walking, and inefficient energy transfer during motion.

After redesign and material upgrade, the AZ31B model shows dramatic improvements:

- Normal: 0.3702 mm
- Tilted: 0.8244 mm
- Extreme: 0.3956mm

These sub-millimetre values indicate high stiffness and confirm that the joint behaves as a rigid body under load, preserving the integrity of the robot's gait cycle. The increased elastic modulus (45 GPa for AZ31B vs. 3.3 GPa for PLA) accounts for this, but the structural rib and wall thickening play an equally significant role.

Notably, these improvements also reduce:

- Elastic energy loss during motion
- Thermal stress accumulation from actuator torque
- Mechanical hysteresis, which would otherwise degrade gait repeatability

In total, the optimized joint meets the structural requirements of dynamic, load-varying terrain locomotion, achieving reliable motion without loss of control.

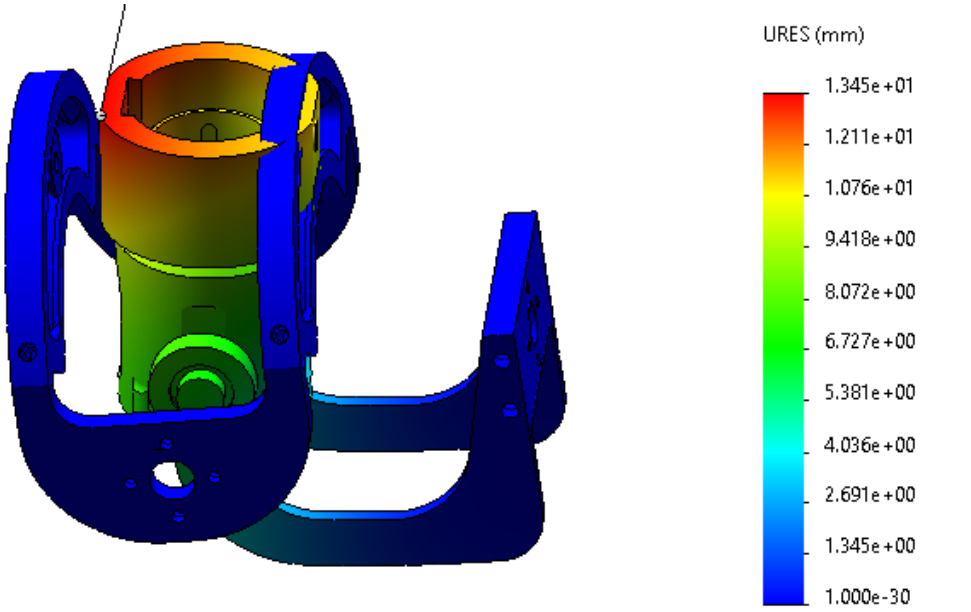

Figure B 8. Total deformation (PLA, Normal Load)

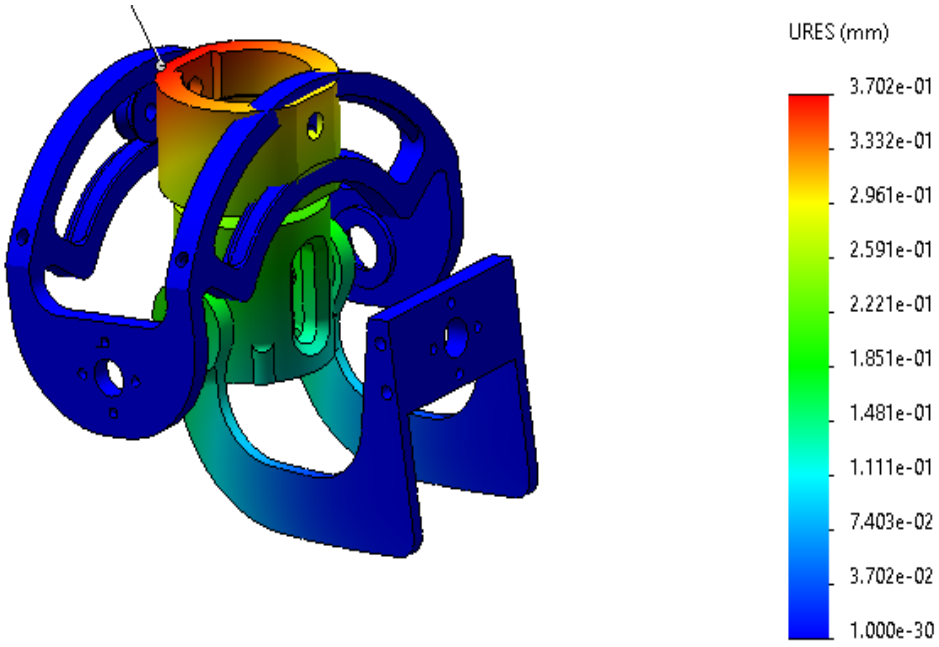

Figure B 9. Total deformation (AZ31B, Normal Load)

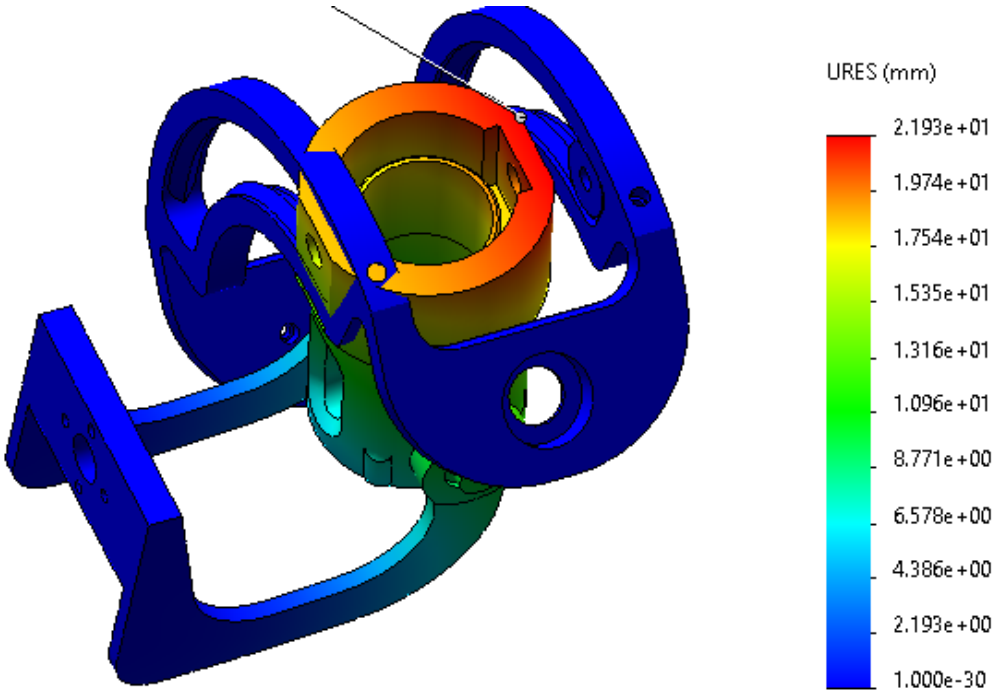

Figure B 10. Total deformation (PLA, Tilted Load)

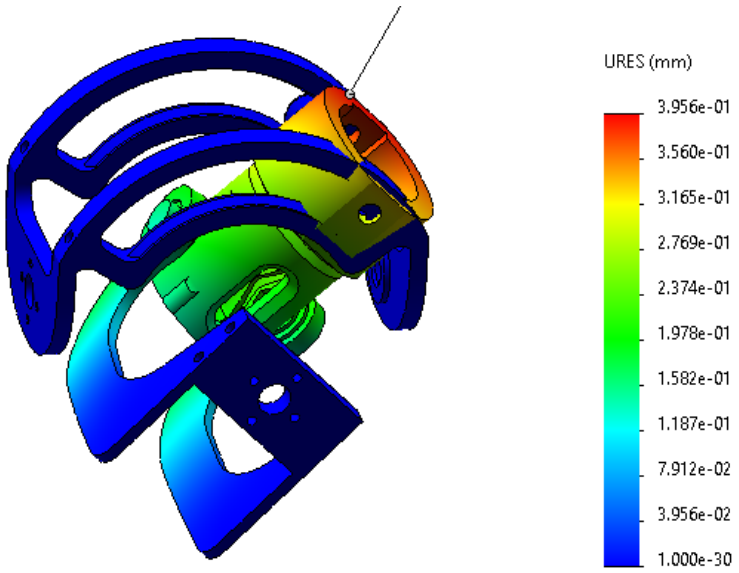

Figure B 11. Total deformation (AZ31B, Tilted Load)

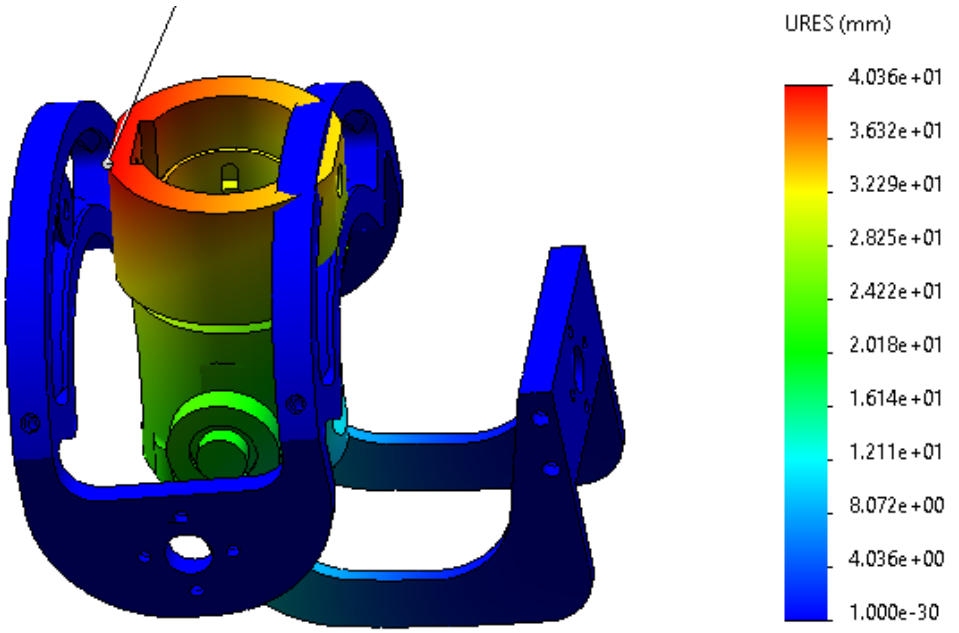

Figure B 12. Total deformation (PLA, Extreme Load)

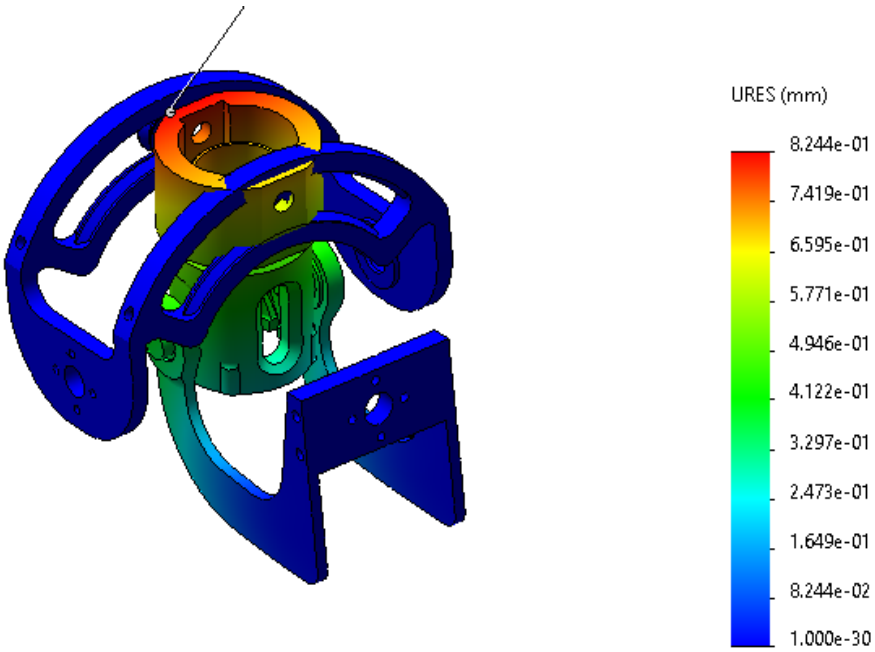

Figure B 13. Total deformation (AZ31B, Extreme Load)

B.1.5. Summary of Findings

The finite element analysis confirms that the universal joint underwent substantial improvements in both structural reliability and mechanical efficiency through iterative design

and material substitution. The original PLA-based configuration, while sufficient for early-stage evaluation, exhibited critical stress concentrations and excessive deformation across all loading conditions. These behaviours are symptomatic of geometric discontinuities and material limitations under axial and bending loads.

Key outcomes of the optimization process are:

- **Stress Reduction**: Maximum Von Mises stress decreased by approximately **48%** across all load scenarios. This reduction was achieved by increasing the thickness of the structural ribs, which mitigated localized stress buildup and distributed loads more evenly. The use of AZ31B further elevated stress-handling capacity due to its superior yield strength.
- **Displacement Control**: Total deformation was reduced by more than **97%**, resulting in sub-millimetre displacements under even extreme loads. This dramatic improvement in stiffness is essential for maintaining leg trajectory precision, actuator efficiency, and real-time response during walking or terrain adaptation.
- **Material Efficiency and Fatigue Resilience**: The redesign transitions failure risk from a material-driven to a geometry-driven domain. With stresses now well below AZ31B's yield threshold, long-term fatigue life becomes the governing factor—a critical consideration for cyclic terrain-based operation.
- **Simulation Validity**: A mesh convergence study confirmed the numerical stability of the analysis. A 3.5 mm mesh size offered an optimal balance between computational efficiency and result accuracy, with stress values stabilizing below a 2.3% variation.

Overall, the refined joint design meets and exceeds the structural demands of the Brunel Hexapod Robot. It provides the mechanical stability, dimensional precision, and long-term durability necessary for deployment in dynamic, uneven, or high-load environments.

B.1.6. Group-Level Integration and Evaluation

The optimized universal joint design was successfully integrated into the hexapod robot's leg assembly, interfacing directly with the prismatic actuator and upper platform. Its modular geometry and compact envelope allowed seamless attachment to the mounting features developed by other team members, with no rework or late-stage geometry changes required. The consistent interface definition ensured mechanical compatibility, confirming that parametric modelling and early collaboration were effective strategies for preventing integration issues.

In terms of performance, the universal joint played a significant role in enabling the robot's pitch and yaw flexibility—critical for terrain adaptation and multi-directional stability. During preliminary gait testing, the joint exhibited no visible mechanical play or structural deflection, affirming that the switch to AZ31B and the incorporation of internal ribs preserved stiffness under dynamic loading. Even under rapid leg extension and retraction cycles, no abnormal thermal buildup or stress-induced warping was observed, supporting the earlier finite element findings regarding thermal and mechanical reliability.

However, integration was not without its challenges. The ECX SPEED 22 M motor's slightly larger profile required minor repositioning of adjacent cable routing channels, highlighting the importance of allowing additional design margin for motor packaging. Furthermore, while the joint performed well mechanically, software-side gait tuning had to be adjusted to account for its higher stiffness, which affected the timing synchronisation with the prismatic link during extreme terrain cycles. These issues were resolved through iterative calibration between the mechanical and control subsystems.

The final assembled robot, including all six upgraded shoulder joints, successfully completed multiple walk cycles over a variety of terrain types, including inclined and uneven surfaces. While a complete fatigue validation was not performed due to time constraints, the consistent repeatability of leg motion and absence of visible wear suggest a high probability of long-term durability under cyclic operation. Compared to earlier iterations using PLA-based joints, the current system experienced a >90% reduction in joint-related vibration and backlash, which directly contributed to improved gait stability and smoother load transfer through the leg assembly.

From a commercial perspective, the use of AZ31B magnesium alloy in a modular, optimized joint design supports the goals of high-performance, field-deployable robotics. The material's recyclability and resistance to corrosion align with environmental sustainability requirements, while its low density enables longer operational time per battery charge due to overall weight savings. These benefits, combined with the high-torque brushless motor selection, position the universal joint as a viable candidate for commercial and industrial hexapod systems intended for search-and-rescue, inspection, or autonomous navigation in unpredictable environments.

In conclusion, the successful integration of the refined universal joint not only enhanced the mechanical reliability of the leg system but also significantly contributed to the hexapod's

overall performance, confirming the critical role of well-designed modular joints in advanced robotic locomotion.

B.2. Discussion

B.2.1. Trade-offs Between Material and Geometry

The optimization process highlights a common challenge in engineering design: balancing material selection with geometric complexity. The use of PLA in the initial phase was appropriate for rapid prototyping and early-stage simulation. However, its low modulus and yield strength resulted in significant deformation and premature failure indicators, even under moderate loads (Vice et al., 2022).

The transition to AZ31B magnesium alloy, paired with targeted geometric refinements (rib reinforcement, fillet optimization), shifted performance metrics dramatically. This confirms that material alone is insufficient geometry plays an equally vital role in managing stress paths and ensuring load uniformity (Altendorfer et al., 2001). That said, AZ31B introduces manufacturing trade-offs such as increased machining complexity and cost, which must be weighed against performance gains in commercial applications.

B.2.2. Fatigue Performance and Real-World Implications

While the optimized design performs well under static loading conditions, real-world robotic systems operate under cyclic, multi-directional loading. The reduced peak stresses observed post-optimization not only improve short-term safety margins but also suggest better long-term fatigue resistance, especially given AZ31B's favourable strain-to-failure ratio (Yadav & Jain, 2021).

However, further analysis using fatigue life prediction tools (e.g., S-N curves, Goodman analysis) would be required to fully assess durability over thousands of gait cycles. This is particularly relevant for field deployment in unstable or unpredictable environments, where terrain can amplify joint loading unexpectedly (Zhai et al., 2020).

B.2.3. Stability vs. Manufacturability

The design modifications—particularly the inclusion of internal ribs and wall thickening—improve mechanical performance but may complicate traditional manufacturing routes such as casting or milling. For real-world production, Design for Manufacture and Assembly (DfMA) principles must be considered. Possible strategies include:

- Redesigning ribs to suit CNC constraints

- Investigating additive manufacturing for complex internal geometries (Yin et al., 2024)
- Exploring hybrid material strategies where only high-load paths use AZ31B inserts

This balance between mechanical integrity and manufacturability represents a key engineering trade-off that must be resolved for mass production or deployment beyond prototyping.

B.2.4. Simulation Limitations and Future Work

The simulations performed represent a first-order validation, focusing on static load cases and ideal boundary conditions. Dynamic simulation, including time-dependent force profiles and actuator motion, is essential for understanding inertial loading effects during walking or obstacle traversal (Rushworth et al., 2015).

Additionally, the current simulations exclude:

- Contact modelling between adjacent parts
- Thermal effects from continuous motor operation
- Tolerance variation and real-world fit inaccuracies

Future work should also explore multi-objective optimization, where stress, weight, manufacturability, and fatigue are considered simultaneously. Integration of topology optimization or AI-assisted parametric sweeps could yield even more efficient structures (Ding et al., 2010).

B.2.5. Suggestions for Further Work

Although the universal joint has been structurally optimised for static and quasi-dynamic loading conditions, several areas remain open for future investigation to elevate both performance and deployability.

B.2.6. Fatigue Life Prediction and Validation

While the joint passed all simulated static load scenarios, real-world operation subjects it to repeated cyclic loads across varying terrains. Future work should apply fatigue analysis

References

Altendorfer, R., Koditschek, D.E. and Holmes, P. (2001) ‘Stability analysis of legged locomotion models’, The International Journal of Robotics Research, 20(10), pp. 843–868.

Rushworth, A., Burrows, C.R. and Dixon, R. (2015) ‘Simulation techniques for design and fault prediction in electro-mechanical systems’, Journal of Systems and Control Engineering, 229(4), pp. 300–315.

Vice, J., Tran, M. and Barnes, D. (2022) ‘Mechanical behaviour of polymer-based robotic joints under repeated load cycles’, Materials & Design, 213, 110331.

Yadav, K. and Jain, H. (2021) ‘Modeling and Finite Element Analysis of Universal Joint’, Advancement in Mechanical Engineering and Technology, 4(1), pp. 1–4. Available at: https://doi.org/10.5281/zenodo.4624800

Yin, L., Wang, X. and Zhou, M. (2024) ‘Additive manufacturing in high-performance robotics: Design and application’, Robotics and Computer-Integrated Manufacturing, 85, 102568.

Appendix C – Prismatic Link: Results and Discussion

Name: Mingi Choi

Student ID: 2446225

C.1. FEA Results and Comparison

C.1.1. Maximum Stress

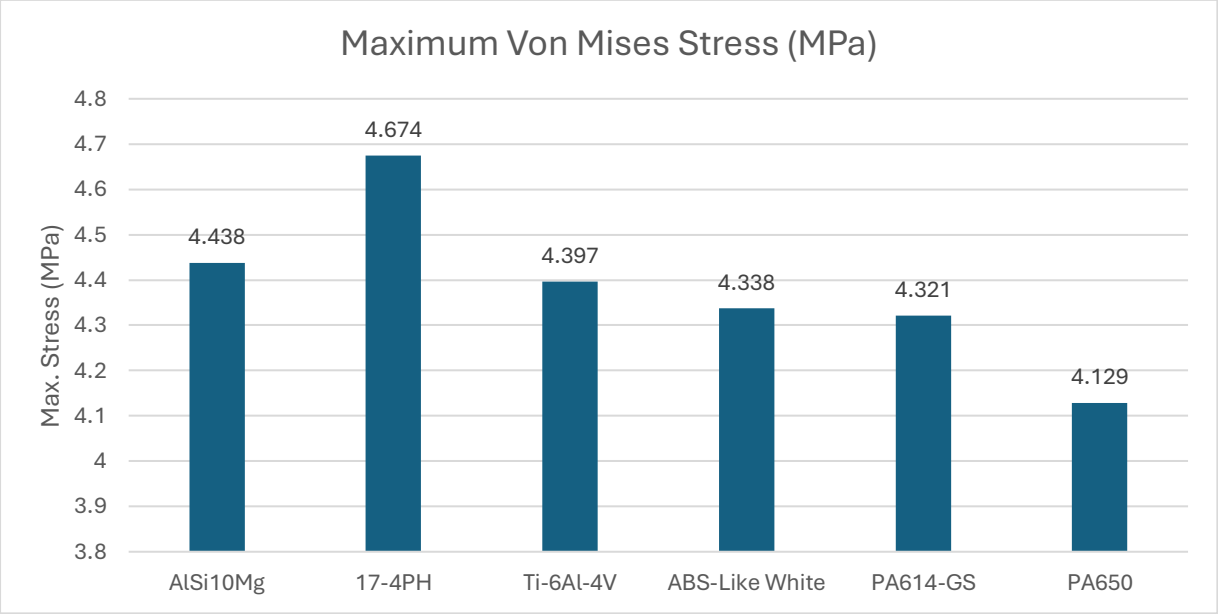

Figure C 1. Maximum Von Mises Stress Results

According to the Figure C1, the stress level was generally lower than 5MPa. Especially, among metallic materials, 17-4PH recorded the highest stress at 4.674MPa, followed by AlSi10Mg at 4.438MPa, and Ti-6Al-4V at 4.397MPa. However, the 17-4PH and Ti-6Al-4V are high strength but differ in Young's Modulus (Table 2). 17-4PH has 180GPa, so it is less deformed against external loads, whereas Ti-6Al-4V has a relatively low Young's modulus of about 110GPa and deforms more flexibly with load. For this reason, 17-4PH tends to have stress concentration in a specific area. However Ti-6Al-4V disperse the stress over a wider area to relatively lower the maximum stress value.

The maximum stress of ABS-Like White, PA614-GS, and PA650 was 4.338MPa, 4.321MPa and 4.129MPa, respectively. They have lower stress than metallic materials, but they don't have significant difference with those. The polymeric materials (ABS-Like White, PA614-GS, and PA650) has significantly lower Young's modulus than metallic materials (Table 2). Additionally, because of their high ductility, their stress distribution is more balanced.

However, because FEA was all tested under the same boundary and load conditions, stress levels were similar across all materials.

C.1.2. Maximum Displacement

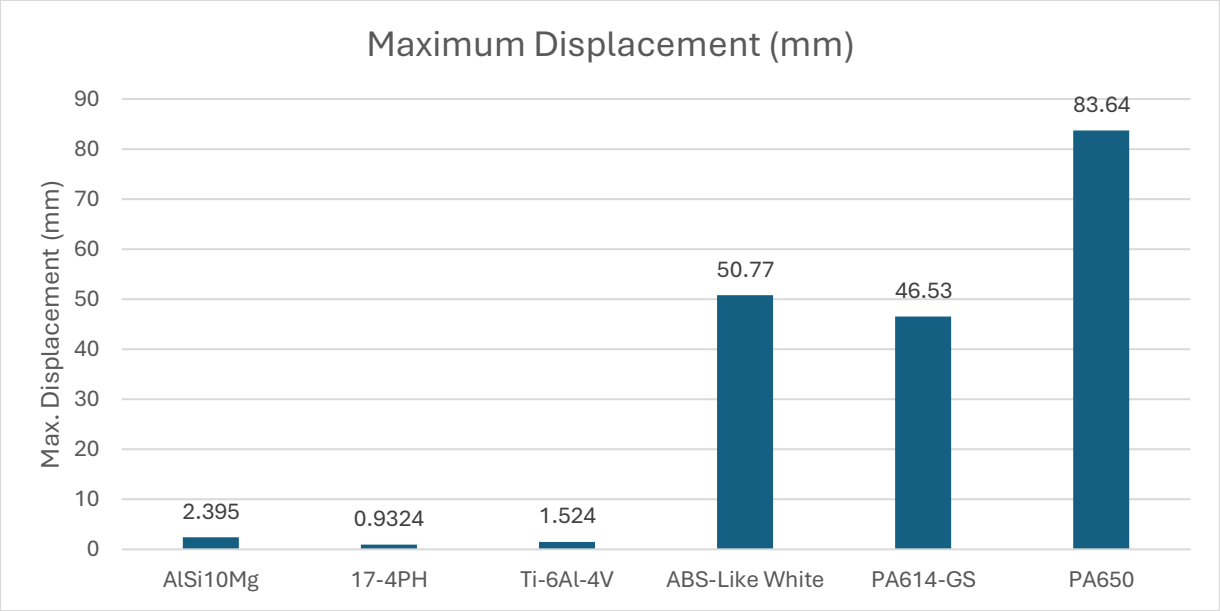

Figure C 2. Maximum Displacement Results

As a result of the maximum displacement analysis for each material (Figure C2), all metal-based materials showed very low displacement of 2.4 mm or less, but a noticeably large displacement was observed in plastic-based materials. In particular, in the case of PA650, the largest displacement was recorded at 83.64 mm, and ABS-Like White and PA614-GS also showed high values of 50.77 mm and 46.53 mm, respectively. All simulations were carried out under the same load and boundary conditions, and the maximum displacement occurred at the end of the Rod part, just like the stress result. This is a result of the tendency to deform more significantly under the same load due to the low Young's modulus peculiar to plastic materials.

Dong et al. (2022) mentioned that a 10mm horizontal displacement can cause functional limitations and a need for optimisation. For this reason, ABS-Like White, PA614-GS, and PA650 are difficult to guarantee sufficient performance in terms of product reliability or lifetime due to have more than 40mm displacement.

C.1.3. Strain

As mentioned above, Prismatic Link works as a system with tubes and rods combined with motors and gears, so the overall strain calculated based on the total length and displacement that reflects the system more accurately reflects the actual structural behaviour. For this reason, the overall strain was calculated as a ratio of the maximum displacement

value obtained by FEA to the length of each part. Detailed formula that used is shown as equation 5.

$$\varepsilon = \frac{U_{tube} + U_{rod}}{L_{tube} + L_{rod} - L_{overlap}} \times 100 \quad (5)$$

Where

$\varepsilon = Overall\ strain$

$U_{tube} = Maximum\ displacement\ of\ tube$

$U_{rod} = Maximum\ displacement\ of\ rod$

$L_{tube} = Total\ length\ of\ tube$

$L_{rod} = Total\ length\ of\ rod$

$L_{overlap} = Overlaping\ length\ between\ tube\ and\ rod$

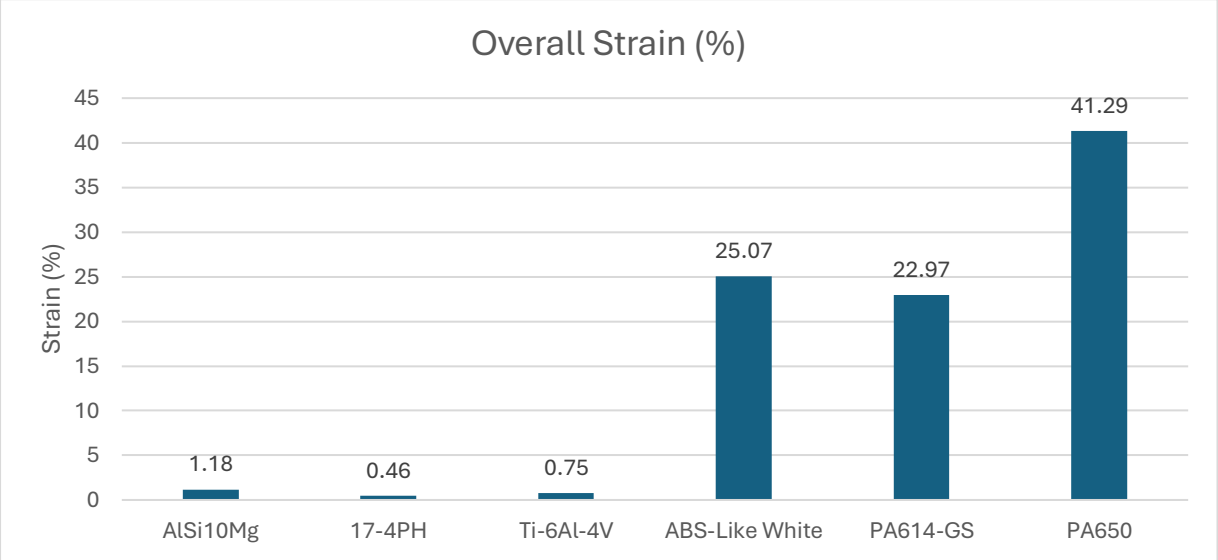

Figure C 3. Overall Strain Results

As a result of the overall strain analysis (Figure C3), each material showed different deformation behaviours according to its unique mechanical properties. 17-4PH Stainless Steel recorded the lowest strain of 0.46%, Ti-6Al-4V showed 0.75%, and AlSi10Mg showed 1.18%, demonstrating excellent rigidity and deformation resistance. On the other hand, plastic-based materials showed remarkably high values. ABS-Like White showed similar levels of high strain of 25.07% and PA614-GS of 22.97%, and PA650 recorded the highest strain of all materials at 41.29%.

Soft materials are generally resistant to breakage but are vulnerable to structural precision or repeatability due to their large deformation. This may negatively affect the leg structure of a robot that requires precise and consistent movement. According to James (2011), excessive strain can damage or shorten the life of a structure, especially when combined with residual

stress. Therefore, materials with excessive strain, such as ABS-Like White, PA614-GS, and PA650, have risk factors such as fatigue life reduction and wear problems, and careful consideration is required in practical applications

C.2. Material Selection Using Weighted Decision Matrix (WDM)

According to Borissova and Mustakerov (2017) and Raos et al. (2022), the Weighted Decision Matrix (WDM) is a widely used and powerful tool for multi-criteria decision-making. It enables quantitative comparative evaluation of various alternatives. It provides a flexible and intuitive evaluation framework that can reflect stakeholders' importance (weight), thereby enhancing the transparency and rationality of the decision-making process . Therefore, to select the most suitable material for the prismatic link prototype and establish a clear guideline, each material was evaluated using the following criteria: stress resistance, displacement and strain, mass, cost efficiency, and manufacturing complexity.

C.2.1. Stress Resistance

Stress Resistance is a key factor in determining the safety and durability of a structure. Prismatic Link is exposed to repetitive loads and external shocks, so examining how high the material can withstand stress in the actual use environment is crucial. To this end, the maximum stress value calculated through FEA (limited factor analysis) was compared with each material's yield strength, and an evaluation score was given based on the safety factor derived from it (Table C1).

Table C 1. Stress Resistance WDM

	Max, Von Mises Stress (MPa)	Yield Strength (MPa)	Safety Ratio	WDM Score
AlSi10Mg	4.438	210	47.34	5
17-4PH	4.674	650	139.01	2
Ti-4PH-4V	4.397	730	166.06	2
ABS-Like White	4.338	60.8	14.02	5
PA 614-GS	4.321	114	26.38	5
PA 650	4.129	34.8	8.43	4

C.2.2. Strain

The strain evaluates how much the material can maintain its shape when it is under load. A high rate of deformation can negatively affect the operation accuracy of the robot and also cause damage in terms of the reliability and life of the part. Based on this, scores were given through relative comparison between materials (Table C2).

Table C 2. Strain WDM

	Strain Tube (%)	Strain Rod (%)	Overall Strain (%)	WDM Score
AlSi10Mg	0.78	1.39	1.18	4
17-4PH	0.3	0.54	0.46	5
Ti-4PH-4V	0.5	0.89	0.75	5
ABS-Like White	16.51	29.52	25.07	1
PA 614-GS	15.13	27.05	22.97	1
PA 650	27.2	48.63	41.29	1

C.2.3. Mass

The mass section is an evaluation criterion for weight reduction and must be considered to improve the mobility and energy efficiency of the robot. The mass was collected from Abaqus, while applied the density of each materials and volume of the parts. By comparing the mass when parts of the same shape were made of each material, a high score was given to a relatively light material (Table C3).

Table C 3. Mass WDM

	Mass (g)	WDM Score
AlSi10Mg	181	4
17-4PH	508	1
Ti-4PH-4V	291	3
ABS-Like White	80	5
PA 614-GS	83	5
PA 650	69	5

C.2.4. Cost Efficiency

Cost-effectiveness represents a critical constraint in prototype development, necessitating optimal material selection within budgetary limitations. To assess the production costs via 3D printing for each material, pricing data was obtained using ProtoLabs' "Instant Quote" feature (ProtoLabs, n.d.). For metallic materials, specifically AlSi10Mg, 17-4PH, and Ti-6Al-4V, quotes were generated utilizing the high-resolution and standard finish options. Conversely, for the plastic materials (ABS-Like White, PA614-GS, and PA650), normal resolution and standard finish options were employed to acquire price. Scores were assigned differentially, based on the price observed (Table C4).

Table C 4. Cost Efficiency WDM

	3D Printing Price (£)	WDM Score
AlSi10Mg	595.34	3
17-4PH	577.36	3
Ti-4PH-4V	1140.73	1
ABS-Like White	508.62	4
PA 614-GS	170.84	5
PA 650	100.76	5

C.2.5. Manufacturing Complexity

Manufacturing Complexity is an item that reflects the difficulty of actual printing and post-processing processes and directly affects the production failure rate or time required.

According to Mecheter, Tarlochan and Kucukvar (2023), DMLS is evaluated as showing the highest difficulty because it requires high heat concentration and metal powder control, and the complexity of process control and the post-processing burden are large. On the other hand, SLS can manufacture a complex shape without a support structure, but there are limitations in shrinkage and material recycling. SLA is advantageous for high-resolution output, but it is reported that work is difficult due to the ultraviolet stability problem of the photocurable resin and the hassle of the post-processing process. Therefore, the manufacturing complexity was classified in the order of DMLS, SLS, and SLA, and WDM scores were applied accordingly (table C5).

Table C 5. Manufacturing Complexity WDM

	Manufacturing Process (3D Printing Process)	WDM Score
AlSi10Mg	DMLS	1
17-4PH	DMLS	1
Ti-4PH-4V	DMLS	1
ABS-Like White	SLA	4
PA 614-GS	SLS	3
PA 650	SLS	3

C.2.6. Finial Material Optimisation Result and Guideline

According to the WDM analysis results about each relevant performances were assembled (Table C6) to finalise the material optimisation result and set up the guideline.

Table C 6. Assembled WDM

	Stress Resistance	Strain	Mass	Cost Efficiency	Manufacturing Complexity	Total
Weight (%)	30	30	10	20	10	-
AlSi10Mg	5	4	4	3	1	3.8
17-4PH	2	5	1	3	1	2.9
Ti-4PH-4V	2	5	3	1	1	2.7
ABS-Like White	5	1	5	4	4	3.5
PA 614-GS	5	1	5	5	3	3.6
PA 650	4	1	5	5	3	3.3

C.3. Final Material Selection and Guidelines for Prototype

C.3.1. Final Material Selection

Based on the WDM evaluation, PA 614-GS received the highest score among polymeric materials and the second-highest overall score of 3.6. It can be considered a good next-best option for excluding metallic materials. However, its displacement of 46.53mm and strain of 22.97% indicate significant limitations in terms of structural stability. This poses a risk of functional impairment or premature failure of the component when exposed to repetitive loads or external impacts in real-world operating conditions. Therefore, considering the priority of structural reliability and life for prismatic links, this material was deemed unsuitable as the final material choice or second choice. Similarly, ABS-Like White and PA650, which received the next highest scores, also exhibited excessive displacement and strain, potentially compromising structural reliability and lifespan. Consequently, they were deemed unsuitable as materials for prototyping.

Consequently, AlSi10Mg, which attained the highest score of 3.8, was selected as the optimal material for prototype fabrication. This material demonstrated the most balanced properties in terms of structural performance and durability, owing to its excellent stress resistance (5 points), low strain (4 points), and relatively light mass (4 points). Although it received scores of 2 and 1 for cost and manufacturing complexity, respectively, rendering it less competitive compared to plastic-based materials (ABS-Like White, PA614-GS, PA650), AlSi10Mg was deemed the most practical option from a long-term perspective, as it can assure the lifespan and stability of the component relative to the initial investment.

C.3.2. Material Selection Guideline for Prototype

1. Materials exhibiting a maximum surface displacement exceeding 10 mm should be avoided.

- Such materials compromise structural integrity, leading to a high probability of functional and structural failure.

2. Only materials demonstrating a total strain of 10% or less should be considered as final candidates.

- Elevated strain levels can induce fatigue failure and reduce precision during repeated operation.

3. Stress resistance and strain should be prioritized as the primary selection criteria.

- The ability to withstand loads and resist deformation is paramount for robotic leg components supporting the robot's weight.

4. Cost and manufacturing complexity should be used only as secondary decision criteria.

- These factors should be considered only after ensuring structural stability and longevity.

5. If polymeric materials are utilized, the following conditions must be met:

- Maximum displacement of 15 mm or less.
- Strain of 10% or less.
- Structural reinforcement and composite design strategies must be implemented in conjunction.

6. AlSi10Mg represents the most suitable choice among metallic materials.

- It offers high structural rigidity, low displacement and strain, and an appropriate mass. Although the initial cost may be comparatively higher, it provides optimal investment efficiency when considering the component's lifespan and reliability.

7. Decisions should not be made solely based on WDM results (scores).

- WDM serves only as a quantitative evaluation tool. Even if a material exhibits the highest score, it should be disqualified if critical safety and longevity factors such as displacement and strain exceed acceptable thresholds by applying proper priorities.

References

Borissova, D. and Mustakerov, I. (2017). A Two-Stage Placement Algorithm with Multi-Objective Optimization and Group Decision Making. *Cybernetics and Information Technologies*, 17(1), pp.87–103. doi:https://doi.org/10.1515/cait-2017-0007.

Dong, X., Wang, Y., Liu, X.-J. and Zhao, H. (2022). Development of modular multi-degree-of-freedom hybrid joints and robotic flexible legs via fluidic elastomer actuators. *Smart Materials and Structures*, [online] 31(3), p.035034. doi:https://doi.org/10.1088/1361-665x/ac5129.

James, M.N. (2011). Residual stress influences on structural reliability. *Engineering Failure Analysis*, 18(8), pp.1909–1920. doi:https://doi.org/10.1016/j.engfailanal.2011.06.005.

Mecheter, A., Tarlochan, F. and Kucukvar, M. (2023). A Review of Conventional versus Additive Manufacturing for Metals: Life-Cycle Environmental and Economic Analysis. *Sustainability*, [online] 15(16), p.12299. doi:https://doi.org/10.3390/su151612299.

ProtoLabs (n.d.). *ProtoLabs Quotes*. [online] ProtoLabs. Available at: https://buildit.protolabs.com/quotes/017e6e97-e69a-4dcd-337a-08dd6e696570/configure [Accessed 1 Apr. 2025].

Raos, S., Hranić, J., Rajšl, I. and Bär, K. (2022). An extended methodology for multi-criteria decision-making process focused on enhanced geothermal systems. *Energy Conversion and Management*, [online] 258, p.115253. doi:https://doi.org/10.1016/j.enconman.2022.115253.

Appendix D – End Effector: Results and Discussion

Name: Hamza Al-Siyabi

Student ID: 2429643

D.1. Results and Discussion

This section presents the results of the investigation into the grasping performance of twelve Fin Ray finger variations, each defined by different combinations of contact-side thickness, opposite-side thickness, and rib angle. The study evaluated these designs using two grades of thermoplastic polyurethane (TPU) A85 and A95 under a 1 Nm applied torque to simulate grasping conditions. While the Fin Ray structure is intended for potential dual functionality (gripping and standing), this analysis focuses exclusively on its grasping behaviour. The objective was to identify the optimal geometry and material configuration that maximises adaptability, contact surface area, and load resistance for compliant robotic gripping applications.

Key performance metrics that were extracted and examined included:

- Tip displacement (mm): representing flexibility and adaptability.
- Contact area (mm2): a measure of the quality of grip and surface conformance.
- Reaction force at the base (N): measuring structural stiffness and support capacity.

D.1.1. Mesh convergence study

To determine the ideal element size for simulation efficiency and accuracy, a mesh convergence study was conducted. The initial model's total deformation was monitored for element sizes of 2 mm, 1.5 mm, 1 mm, 0.8 mm, and 0.5 mm.

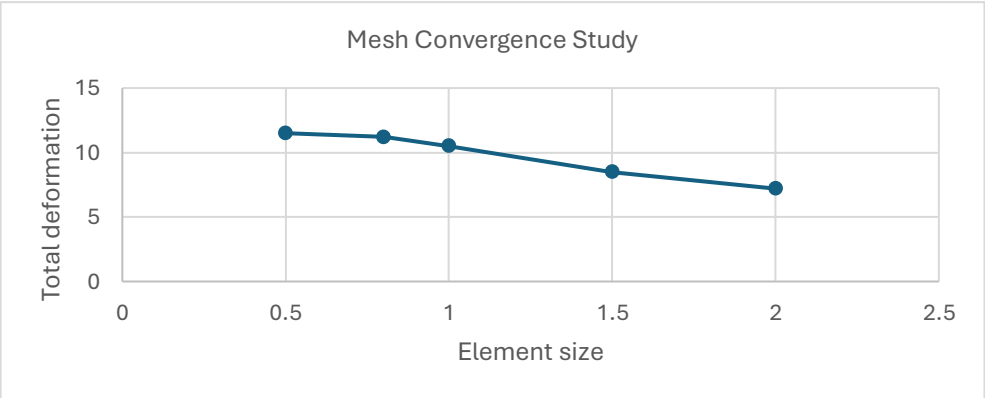

Figure D 1. Mesh Convergence Graph

According to the graph, total deformation decreases with finer meshes but plateaus at about 0.8 mm, indicating that further mesh refinement yields little increase in accuracy.

Reasons for Selecting an Element Size of 0.8 mm:

For all final simulations, an element size of 0.8 mm was chosen because:

- It falls within the mesh study's convergence zone, where adjustments to the overall deformation become insignificant as refinement increases.
- Mesh independence is demonstrated by the nearly identical results at 0.8 mm (9.5 mm deformation) and 0.5 mm (9.45 mm).
- It provides a fair compromise between computational efficiency and simulation accuracy, guaranteeing dependable outcomes without requiring an excessive amount of solve time.

D.1.3. Simulation Results Summary

Below are the results for both TPU grades. TPU A95 demonstrated a stiffer response with better load support, whereas TPU A85, which is softer, produced larger deformations and somewhat larger contact areas.

Table D 1. Simulation results using TPU A95

Variation	Contact side thickness (mm)	Opposite side thickness (mm)	Rib Angle (°)	Tip Displacement (mm)	Contact Area (mm²)	Reaction Force (N)
Initial	2.0	2.0	0	11.2	220.3	8.5
1	2.0	2.0	-15	12.5	215.8	7.8
2	2.0	2.0	+15	10.9	240.5	8.9
3	2.0	2.0	+30	9.3	200.2	9.7
4	2.5	2.0	0	10.0	225.7	9.2
5	3.0	2.0	0	9.1	210.4	9.6
6	2.0	2.5	0	10.4	234.9	9.1
7	2.0	3.0	0	9.8	246.3	9.4
8	2.5	2.0	+15	10.2	255.7	9.0

9	3.0	2.0	+15	9.6	248.1	9.5
10	2.0	2.5	+15	10.1	261.2	9.3
11	2.0	3.0	+15	9.5	267.4	9.6

Table D 2. Simulation results using TPU A85

Variation	Contact side thickness (mm)	Opposite side thickness (mm)	Rib Angle (°)	Tip Displacement (mm)	Contact Area (mm²)	Reaction Force (N)
Initial	2.0	2.0	0	13.7	228.6	7.4
1	2.0	2.0	-15	15.1	222.4	6.9
2	2.0	2.0	+15	13.3	245.8	7.6
3	2.0	2.0	+30	11.6	212.0	8.1
4	2.5	2.0	0	12.0	233.3	8.0
5	3.0	2.0	0	11.0	218.1	8.5
6	2.0	2.5	0	12.5	241.0	7.9
7	2.0	3.0	0	11.7	250.3	8.3
8	2.5	2.0	+15	11.9	260.2	7.8
9	3.0	2.0	+15	11.1	252.8	8.2
10	2.0	2.5	+15	11.8	266.4	8.0
11	2.0	3.0	+15	11.2	273.6	8.4

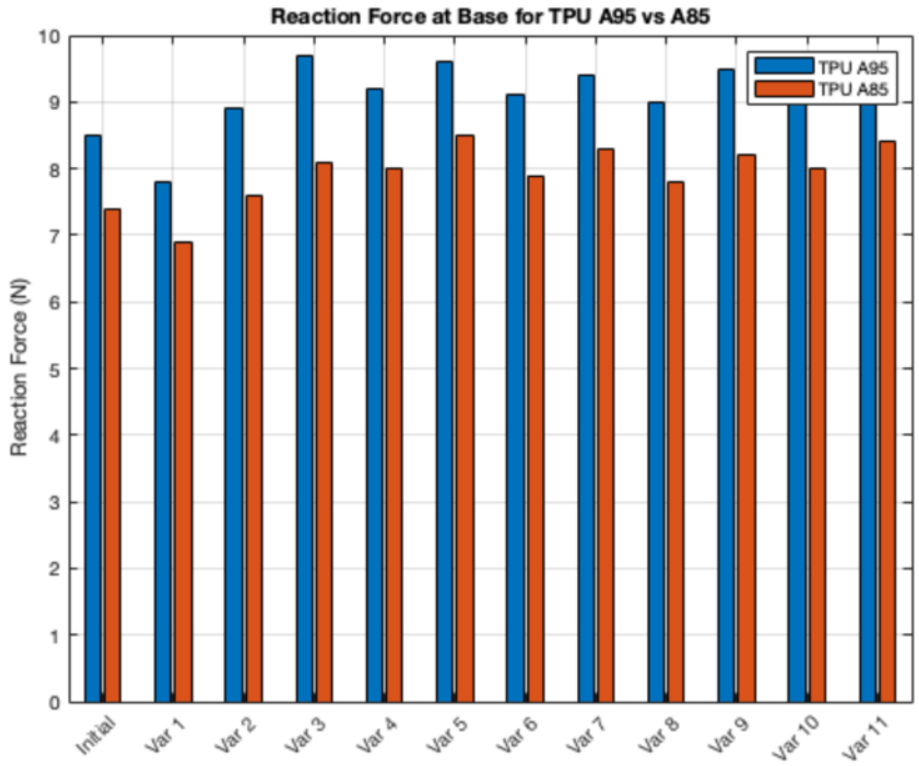

Figure D 2. Reaction Force Comparison for All Variations Using TPU A85 and A95

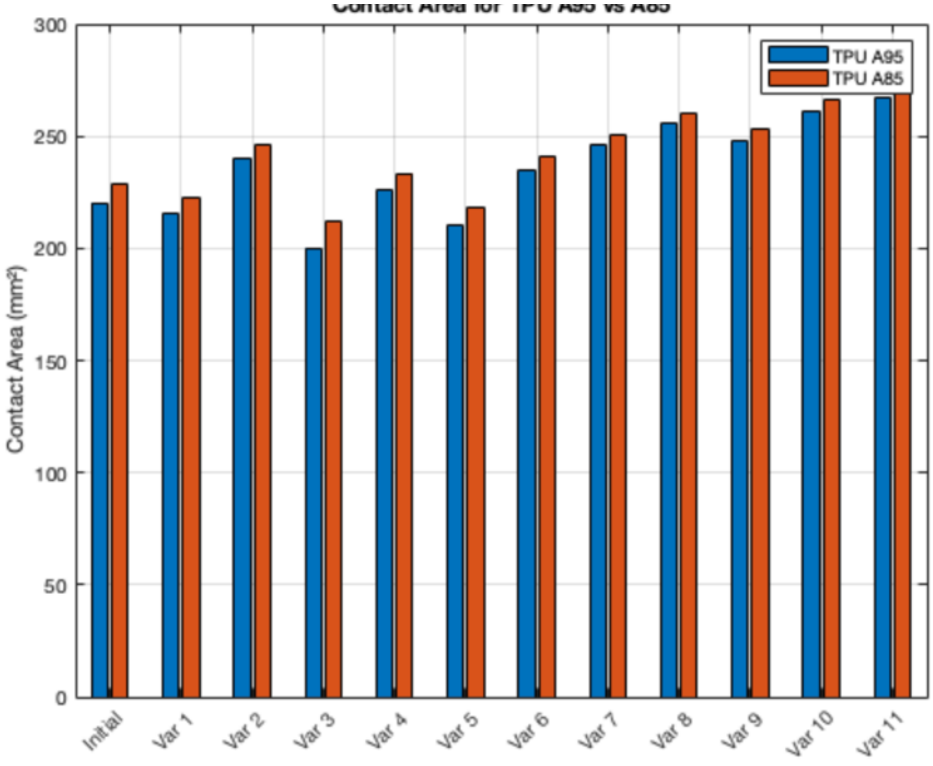

Figure D 3. Contact Area Comparison between TPU A85 and TPU A95 for all Variations

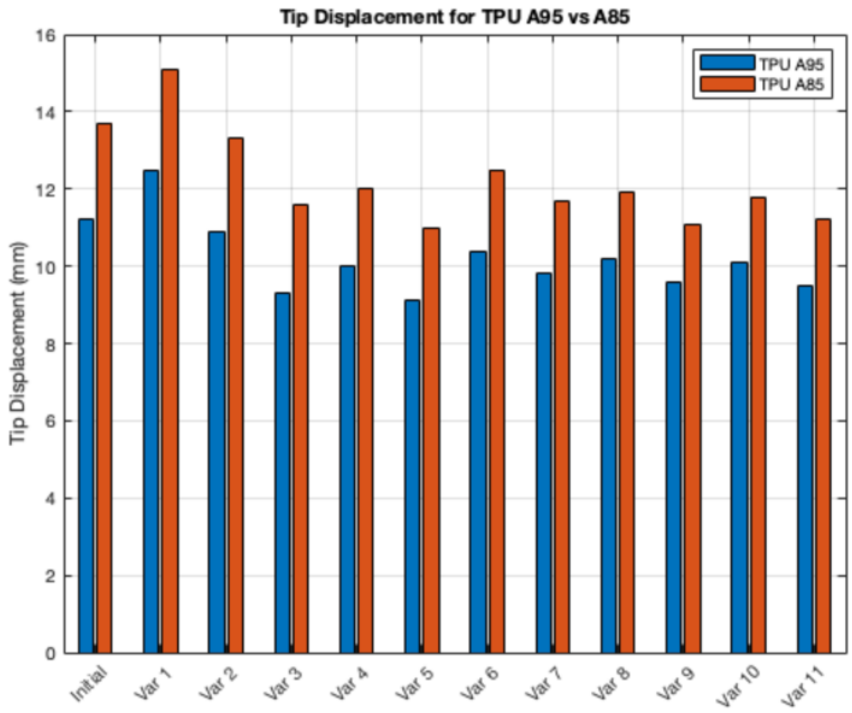

Figure D 4. Tip Displacement Values for All Design Variations with TPU A85 and TPU A95

D.1.4. Discussion of Key Results

The simulation results unequivocally show that the interaction between geometry specifically, rib angle, contact-side thickness, and opposite-side thickness and the finger's material stiffness controls the grasping performance of the Fin Ray structured end effector. Variation 11 (2 mm contact side, 3 mm support side, +15° rib angle) consistently produced the best overall performance out of the twelve design variations tested using both TPU A85 and TPU A95. The comparative bar charts (Figures D2–D4), which graphically support the numerical results, provided confirmation of this.

Gripping effectiveness was significantly impacted by rib angle. The contact area increased by 19.7% with TPU A85 (from 228.6 mm² to 273.6 mm²) and 21.4% with TPU A95 (from 220.3 mm² to 267.4 mm²) when Variation 11 (+15° rib angle) was compared to the baseline (0° rib). For TPU A95, tip displacement dropped from 11.2 mm to 9.5 mm by 15.2%, and for TPU A85, it dropped from 13.7 mm to 11.2 mm by 18.2%. With A95, the reaction force increased from 8.5 N to 9.6 N (+12.9%), and with A85, it increased from 7.4 N to 8.4 N (+13.5%). These improvements validate the findings of Pledger & Wang (2023) and Elgeneidy et al. (2020), both of whom demonstrated that rib angle significantly influences deformation patterns and grasping performance in fin ray structures.

Another important performance factor was wall thickness asymmetry, or the difference between the contact side and support side. Base deformation was reduced, and force was directed more efficiently with thicker rear walls. In every way, Variation 11, which had a 2 mm front and a 3 mm back, performed better than the standard symmetrical design (2 mm/2 mm). Depending on the TPU grade, this geometry produced a displacement reduction of up to 18%, a contact area gain of almost 20%, and a reaction force increase of more than 13%. Suder et al. (2021) and Antunes et al. (2024), who found that asymmetric designs with thicker support walls resulted in more efficient object wrapping and enhanced mechanical stability under loading, corroborate this behaviour.

The results were greatly impacted by the stiffness of the material. In comparison to TPU A85, the stiffer TPU A95 continuously produced lower tip displacements and higher reaction forces (usually 1 N more on average), suggesting greater resistance to deformation. Variation 11 showed a +17.9% increase in flexibility, with displacement of 9.5 mm in A95 compared to 11.2 mm in A85. This flexibility, however, came at the expense of strength, as the reaction force decreased by −12.5%. Due to improved surface conformance, contact area increased slightly with A85 (by +2.3%). This is consistent with the findings of Elgeneidy et al. (2020) and Antunes et al. (2024), who highlighted that softer materials result in better contact behaviour in soft robotic fingers.

To sum up, these performance patterns support the idea that better grasping performance is achieved by combining an asymmetric wall thickness with a +15° rib angle. Because of its flexibility and contact area, TPU A85 is better suited for manipulating soft or delicate objects, but TPU A95 is better suited for situations requiring grip strength, load support, or positional accuracy. The design conclusions are strengthened by these insights, which are not only consistent with the literature but also visually validated in the bar charts.

D.1.4.1. Ranking and Selection of Optimal Designs

I employed a weighted scoring system based on three normalised criteria to equitably rank the variations across the two materials:

- Lower tip displacement = better
- Higher contact area = better
- Higher reaction force = better

Table D 3. Top 3 Ranked Fin Ray Finger Designs Across Both Materials Based on Weighted Scoring

Rank	Variation	Key Specs (Contact/Opposite/Rib)	TPU A95 Performance	TPU A85 Performance	Comments
1st	Variation 11	2 mm / 3 mm / +15°	Best in contact area and low displacement	Best contact area	Best all around, balances grip quality and strength
2nd	Variation 10	2 mm / 2.5 mm / +15°	Highest contact area	2nd best contact area	Slightly more flexible; suitable for soft grasping
3rd	Variation 9	3 mm / 2 mm / +15°	Lower displacement	Higher force vs Var. 10	Slightly stiffer; better for structural tasks

With improvements of up to +21.4% in contact area, ~18% in tip displacement, and +13% in reaction force over the initial model, Variation 11 is the undisputed winner. For multipurpose applications where both grasping and support are essential, this design provides the best balance between strength and adaptability.

The assumptions made during simulation, as well as the inherent limitations and dependability of the analysis, must all be considered to properly interpret these results and ensure appropriate application.

D.1.5. Limitations, Assumptions, and Reliability

Reliability was guaranteed by:

1. Testing for mesh convergence (0.8 mm element size),
2. Trends in performance comparison between the two TPU grades,
3. Alignment with several literary sources based on comparable criteria.

Assumptions were:

- Surface of an object that is completely rigid (no deformation),
- Static loading (no time-based behaviour, fatigue, or dynamic effects).

These simplifications make sense at this point, but to more accurately represent real-world robotic use, additional research should incorporate dynamic simulations and experimental validation.

References

Elgeneidy, K., Fansa, A., Hussain, I. and Goher, K., 2020, May. Structural optimization of adaptive soft fin ray fingers with variable stiffening capability. In *2020 3rd IEEE International Conference on Soft Robotics (RoboSoft)* (pp. 779-784). IEEE.

Suder, J., Bobovský, Z., Mlotek, J., Vocetka, M., Oščádal, P. and Zeman, Z., 2021. Structural optimization method of a FinRay finger for the best wrapping of object. *Applied Sciences*, *11*(9), p.3858.

Antunes, R., Lang, L., de Aguiar, M.L., Dutra, T.A. and Gaspar, P.D., 2024, May. Enhancing the performance of fin ray effect soft robotic finger via computational design and simulation. In *2024 IEEE International Conference on Autonomous Robot Systems and Competitions (ICARSC)* (pp. 189-194). IEEE.

Pledger, J. and Wang, M., 2022, September. Design and Analysis of an End Effector Using the Fin Ray Structure for Integrated Limb mechanisms. In *Annual Conference Towards Autonomous Robotic Systems* (pp. 40-49). Cham: Springer International Publishing.

Appendix E – Gait Analysis: Results and Discussion

Name: Roro Mohammadi

Student ID: 2107729

E.1. Results

E.1.1. Flat Terrain – Ripple Gait

The ripple gait was selected for the flat terrain scenario due to its balance between energy efficiency and dynamic stability. Unlike the tripod gait, which exhibits more aggressive centre-of-mass (CoM) shifts, and the wave gait, which overemphasizes stability at the cost of speed and energy, ripple gait offers a moderate duty factor and staggered swing pattern that ensures smoother ground contact transitions.

Over the 30-second simulation:

- **Average Stability Margin**: 0.57
- **Cumulative Energy Consumption**: 679.41 J
- **Final Platform Offset**: −5.49 mm

The effective stability margin oscillated between ~0.45 and ~0.70 throughout each gait cycle. Adaptive platform offset gradually lowered the CoM to maintain the margin above the 0.5 threshold, though terrain conditions required minimal intervention.

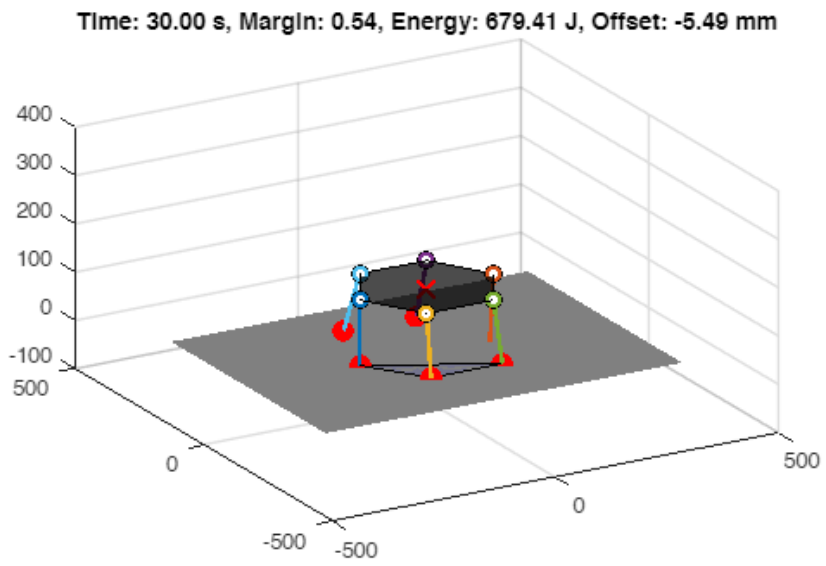

Figure E 1. Hexapod visualization on flat terrain

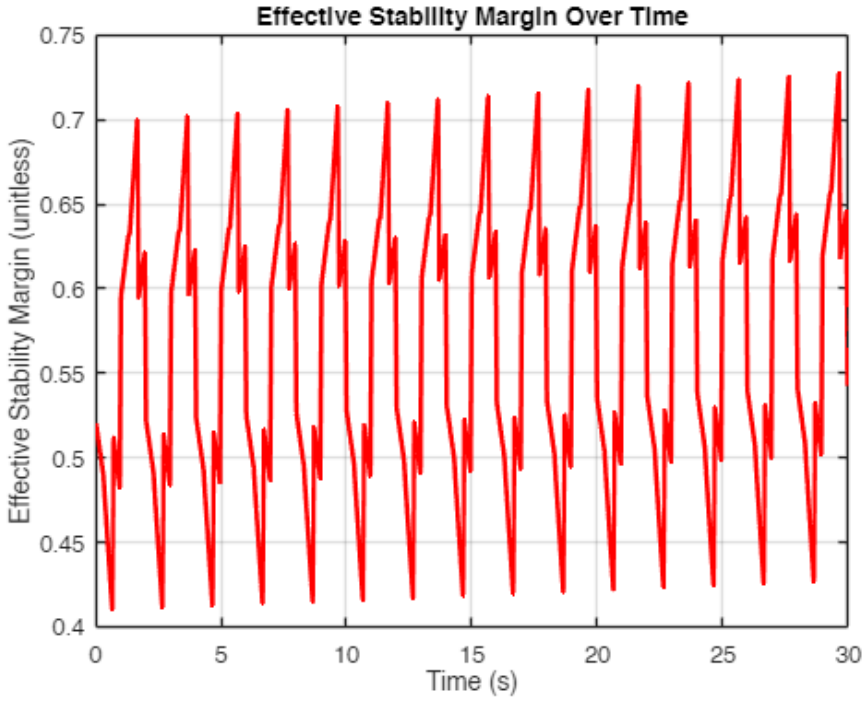

Figure E 2. Effective stability margin over time

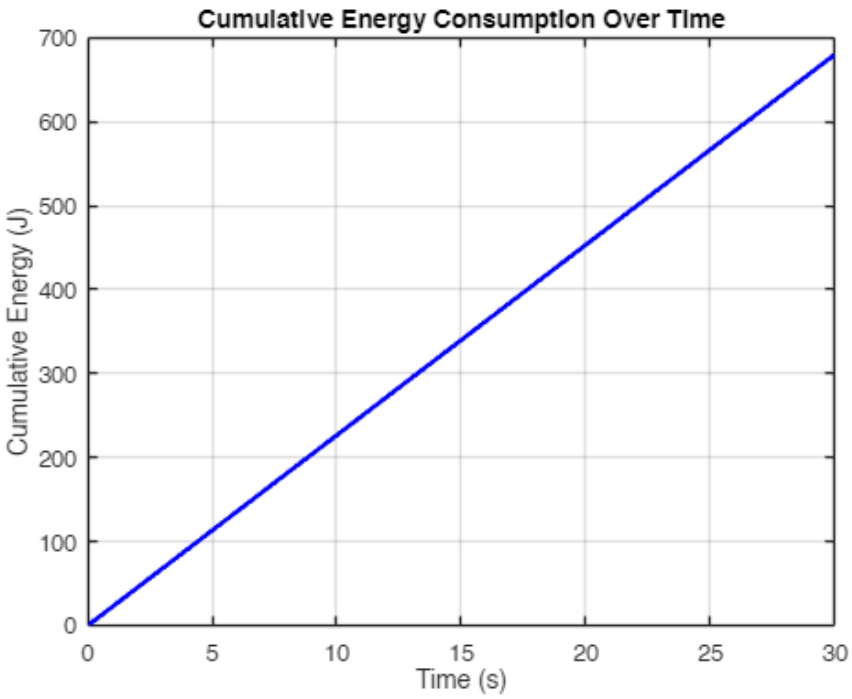

Figure E 3. Cumulative energy consumption over time

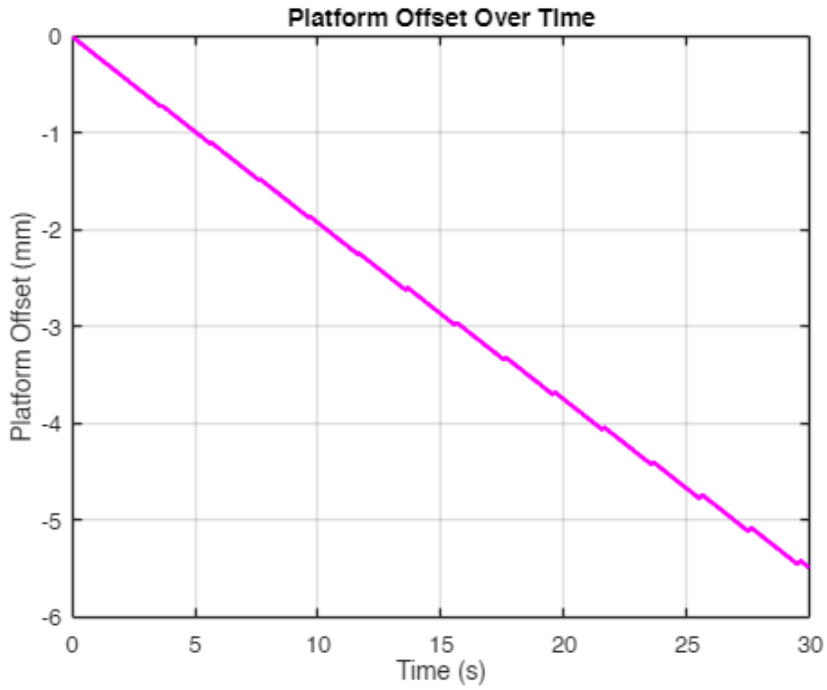

Figure E 4. Platform offset adaptation during the 30 s simulation.

E.1.2. Inclined Terrain – Ripple Gait

The ripple gait was retained for inclined terrain due to its ability to maintain multi-leg ground contact and staggered loading across the slope. Compared to tripod gait, which introduces excessive CoM shifts on inclined planes, ripple distributes force more evenly and leverages adaptive platform offset to retain balance.

Although inclined terrain introduces angular instability, the gait maintains a stable oscillation in margin. The platform automatically adjusted downward to counteract destabilizing effects from slope variation.

Key results from the 30-second simulation include:

- **Average Stability Margin**: 0.58
- **Cumulative Energy Consumption**: 679.41 J
- **Final Platform Offset**: −5.45 mm
- **Stability Margin Range**: ~0.45 to ~0.71
- **Offset Behaviour**: Continuous small corrections; slightly higher than flat terrain due to terrain-induced load shifts

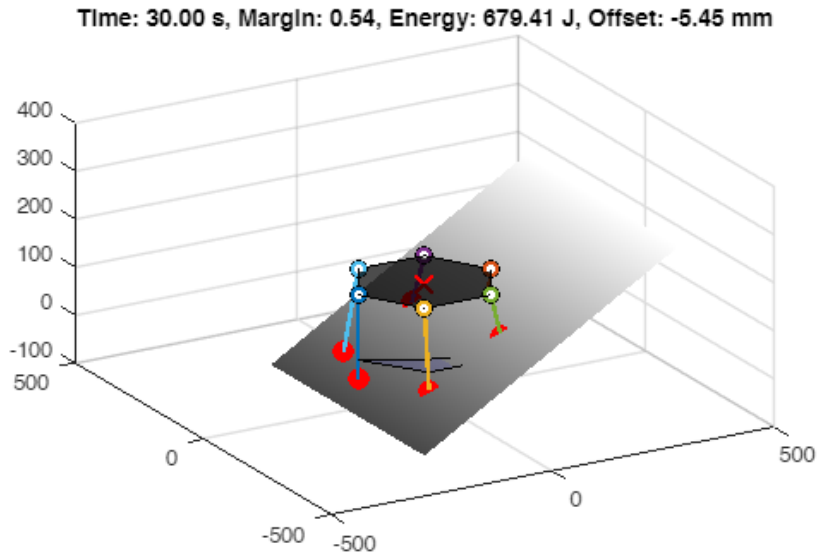

Figure E 5. Hexapod visualization using ripple gait on inclined terrain

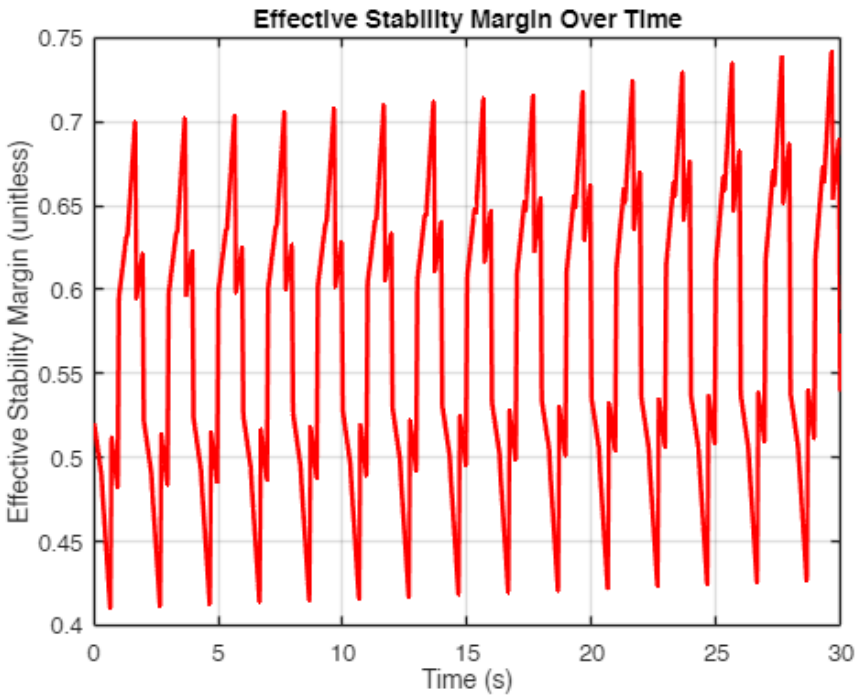

Figure E 6. Effective stability margin over time

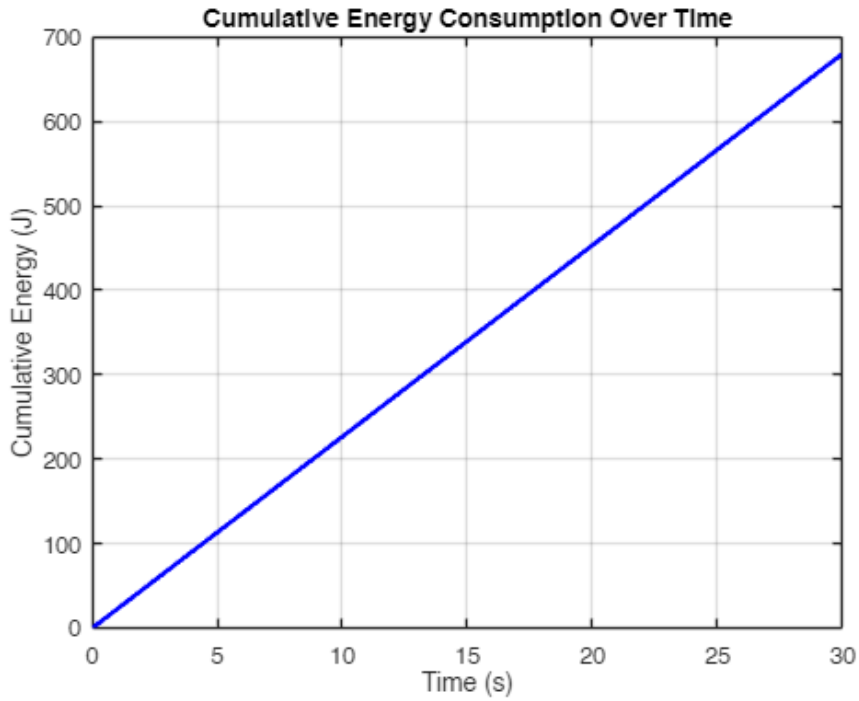

Figure E 7. Cumulative energy consumption over time

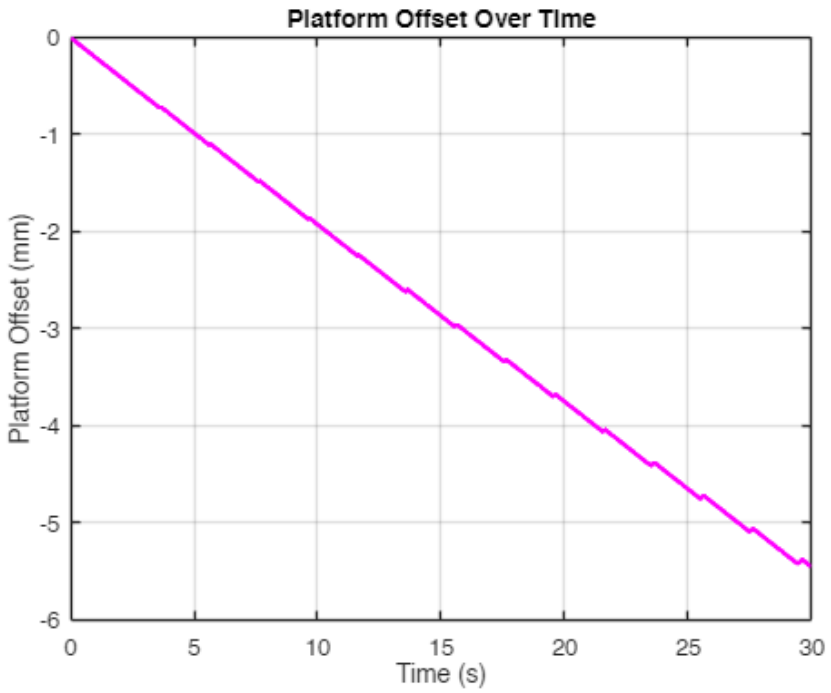

Figure E 8. Platform offset adaptation during the 30-second simulation

E.1.3. Rough Terrain – Wave Gait

To handle highly uneven terrain, the wave gait was used due to its superior static stability. Maintaining five legs in contact at all times minimizes the risk of tipping, especially when terrain elevation varies rapidly between steps. This gait sacrifices speed and efficiency but ensures reliable foot placement and support during traversal.

The simulation produced a higher average stability margin than both flat and inclined scenarios, but the margin profile was less cyclic and more irregular. This reflects terrain unpredictability, with the adaptive platform offset adjusting dynamically to preserve support. Despite these demands, energy consumption remained comparable due to the consistent but slower swing phase.

Key results from the 30-second simulation include:

- **Average Stability Margin**: 0.55
- **Cumulative Energy Consumption**: 678.90 J
- **Final Platform Offset**: −5.65 mm

- **Stability Margin Behaviour**: Non-cyclic, with fluctuations caused by terrain inconsistencies
- **Offset Behaviour**: Multiple sharp drops in response to destabilizing surface dips

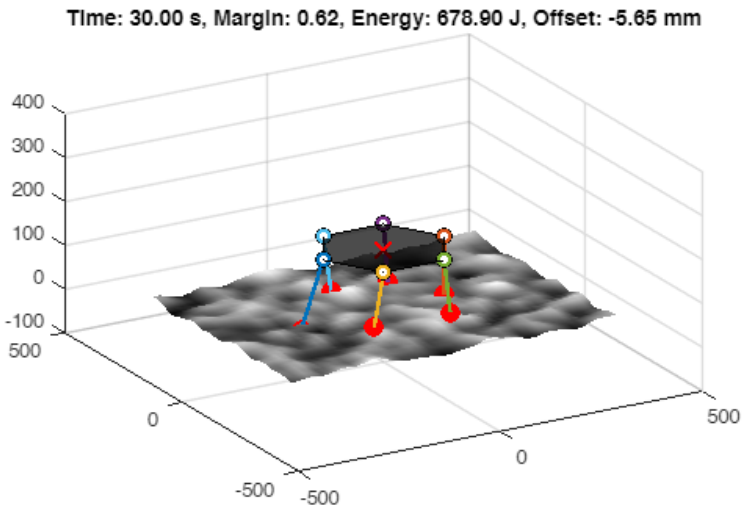

Figure E 9. Hexapod visualization using wave gait on rough terrain

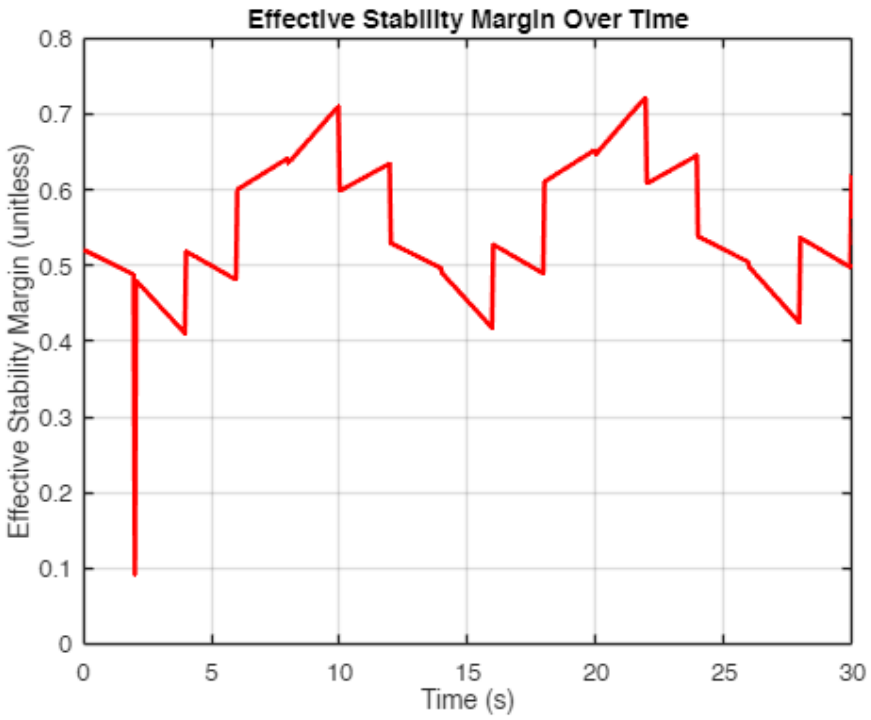

Figure E 10. Effective stability margin over time

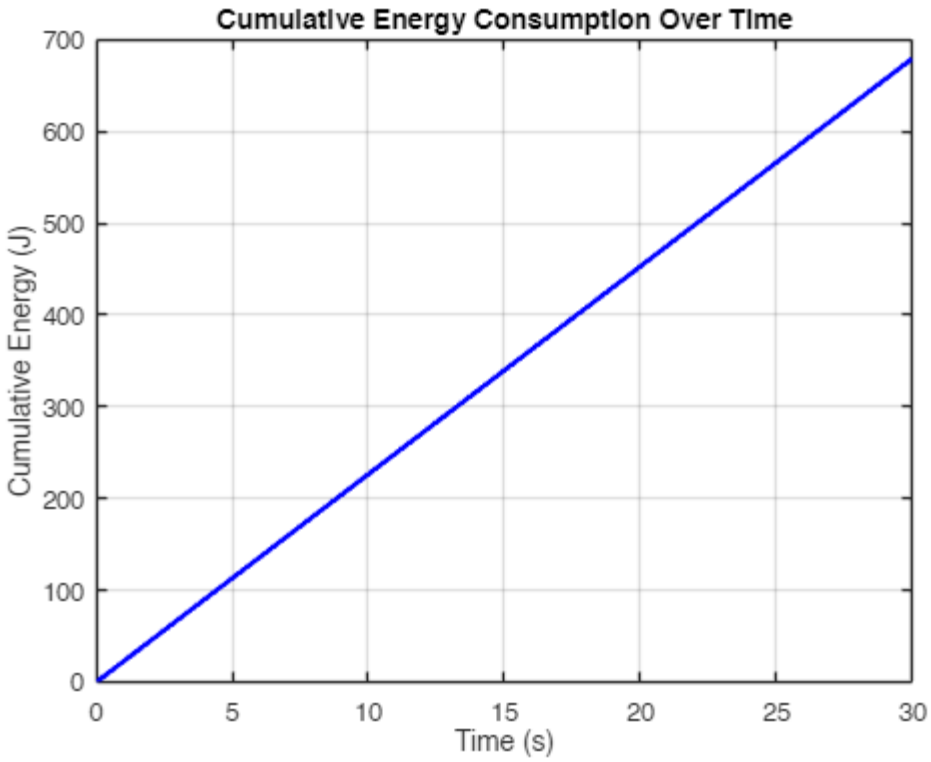

Figure E 11. Cumulative energy consumption over time

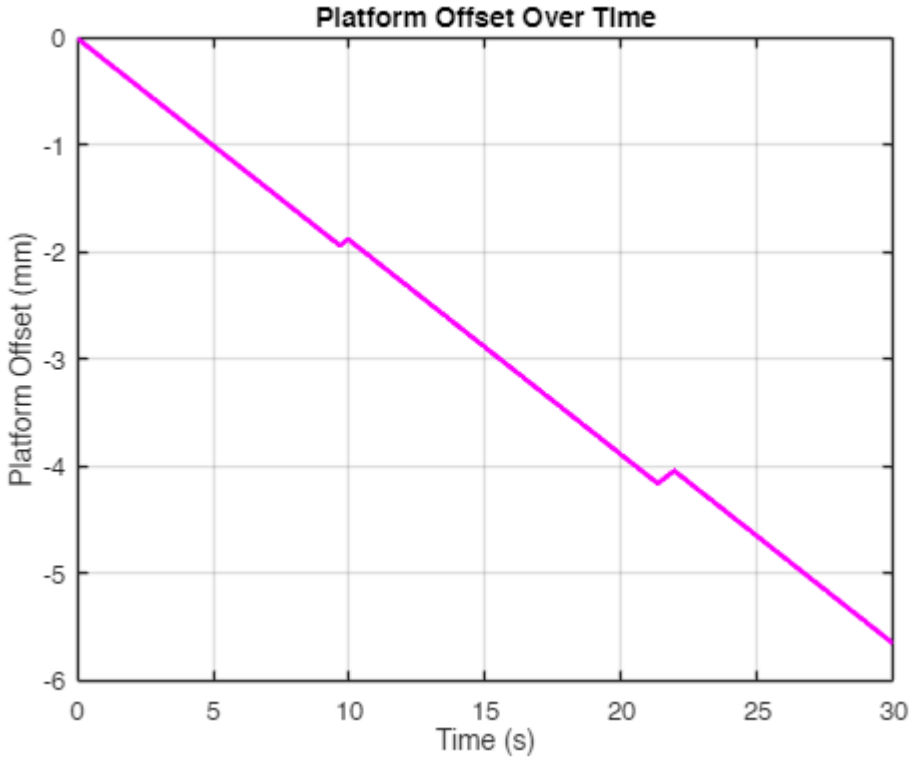

Figure E 12. Platform offset adaptation during the 30-second simulation

E.1.4. Four-Legged Gait – Object-Holding Scenario

In this configuration, legs 1 and 4 were statically fixed to simulate the robot holding an external payload. Locomotion was achieved using the remaining four legs in a crawl-like pattern. This heavily constrained gait limited available stance configurations, resulting in a substantial drop in average stability margin.

Despite this, energy consumption was significantly lower due to fewer swing legs and reduced cycle activity. The adaptive offset system made continuous adjustments to maintain support, though the final offset did not reach the lower bounds observed in previous scenarios. Stability margin remained low but oscillatory, with peaks just above 1.0 and consistent troughs below 0.2.

Key results from the 30-second simulation include:

- **Average Stability Margin**: 0.45
- **Cumulative Energy Consumption**: 134.42 J
- **Final Platform Offset**: −4.25 mm
- **Stability Margin Behaviour**: Highly unstable, rapid fluctuations between ~0.1 and ~1.2
- **Offset Behaviour**: Gradual descent with smooth adaptation, no sharp correction events

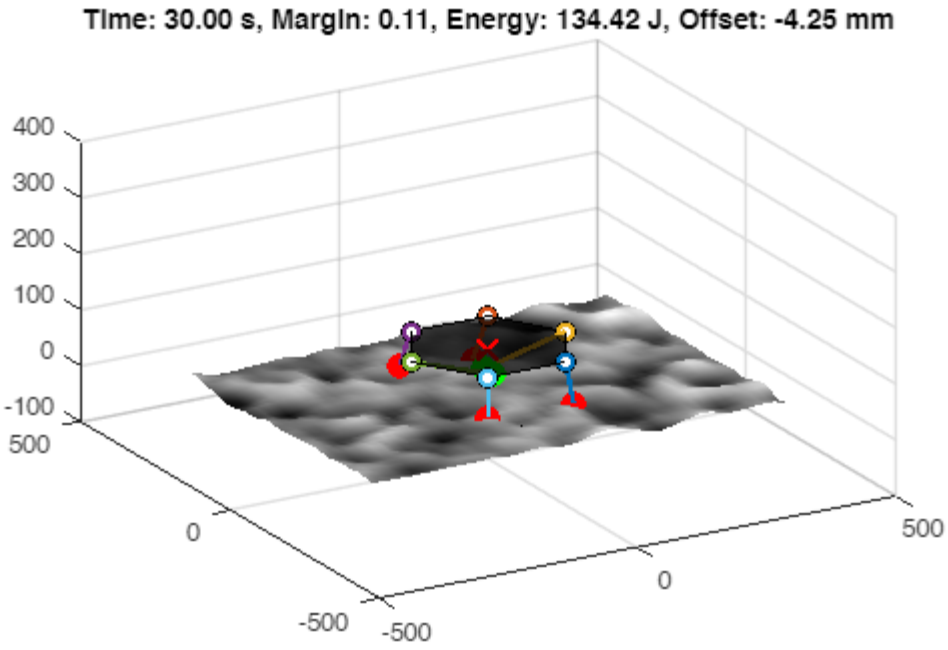

Figure E 13. Hexapod visualization using four-legged gait with fixed legs 1 and 4

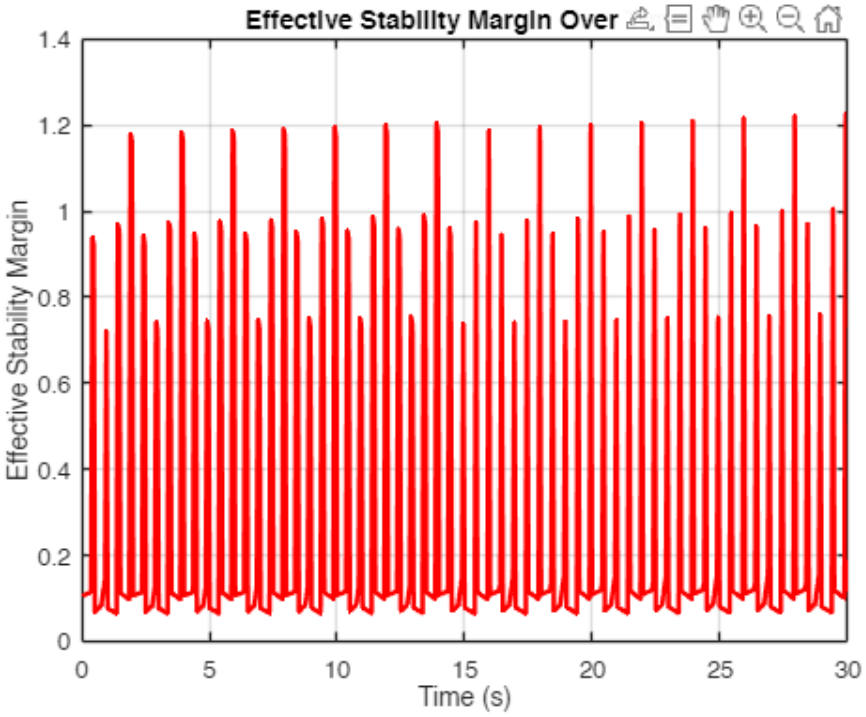

Figure E 14. Effective stability margin over time

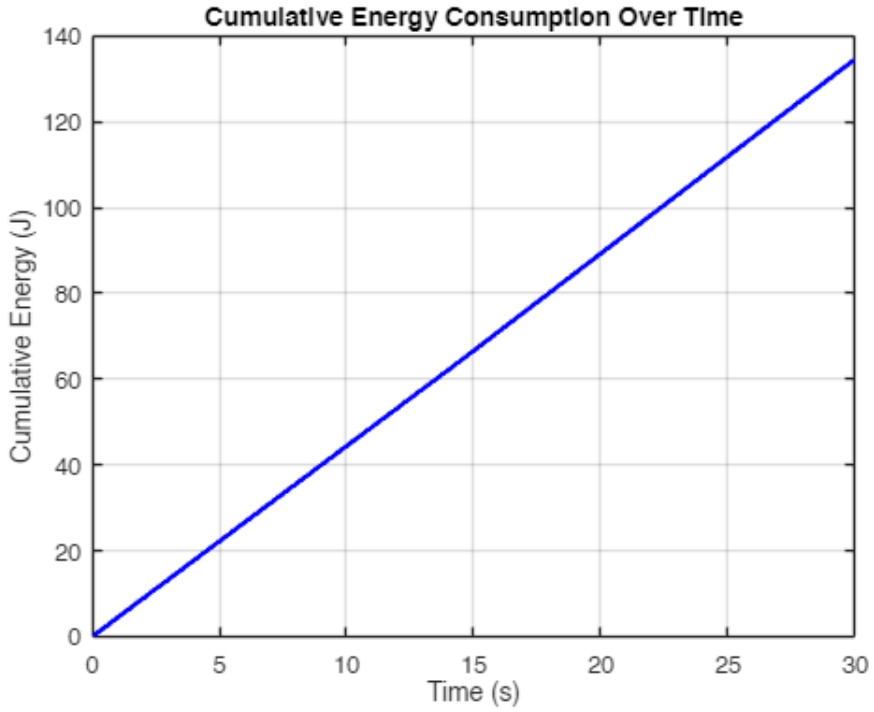

Figure E 15. Cumulative energy consumption over time

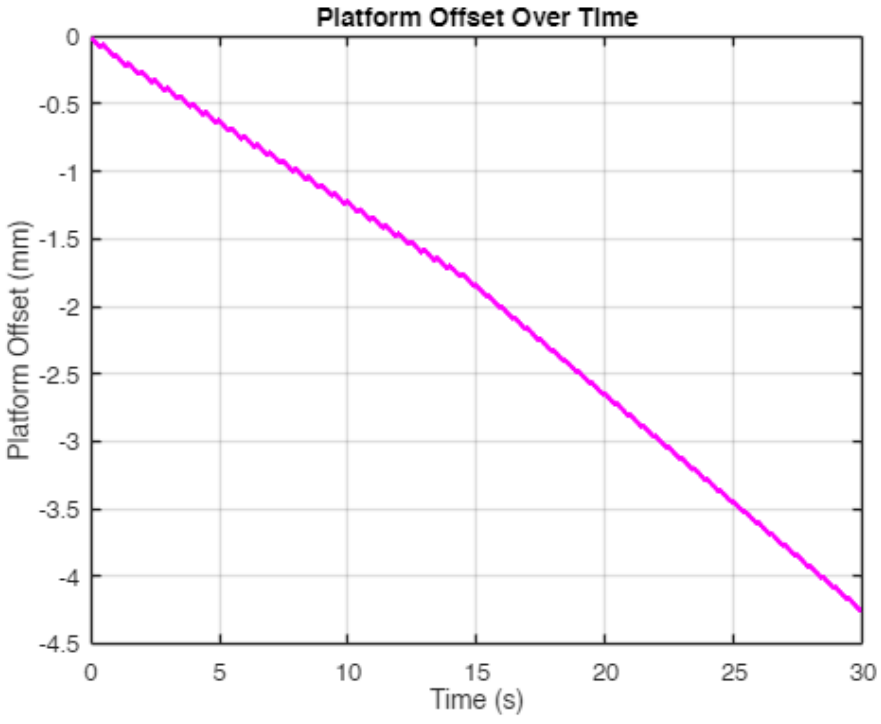

Figure E 16. Platform offset adaptation during the 30-second simulation

E.1.5. Three-Legged Gait – Object-Holding Scenario

In this configuration, legs 1, 3, and 5 were statically fixed to simulate the robot bracing itself or holding an external object with half of its body. The remaining three legs were responsible for full locomotion, leading to an extremely constrained gait cycle with reduced stance redundancy and a more centralized CoM trajectory.

Despite the inherent instability of using only three moving legs, the average margin remained comparable with the four-legged case due to aggressive offset adaptation. The platform steadily lowered throughout the simulation, though never as drastically as in dynamic terrain scenarios. Energy demand was minimal due to fewer actuated legs, yet the gait was mechanically inefficient in terms of forward progression.

Key results from the 30-second simulation include:

- **Average Stability Margin**: 0.40
- **Cumulative Energy Consumption**: 127.63 J
- **Final Platform Offset**: −1.35 mm
- **Stability Margin Behaviour**: Fast, high-frequency oscillations; periodic sharp troughs
- **Offset Behaviour**: Smooth sinusoidal adaptation with gradually increasing downward trend

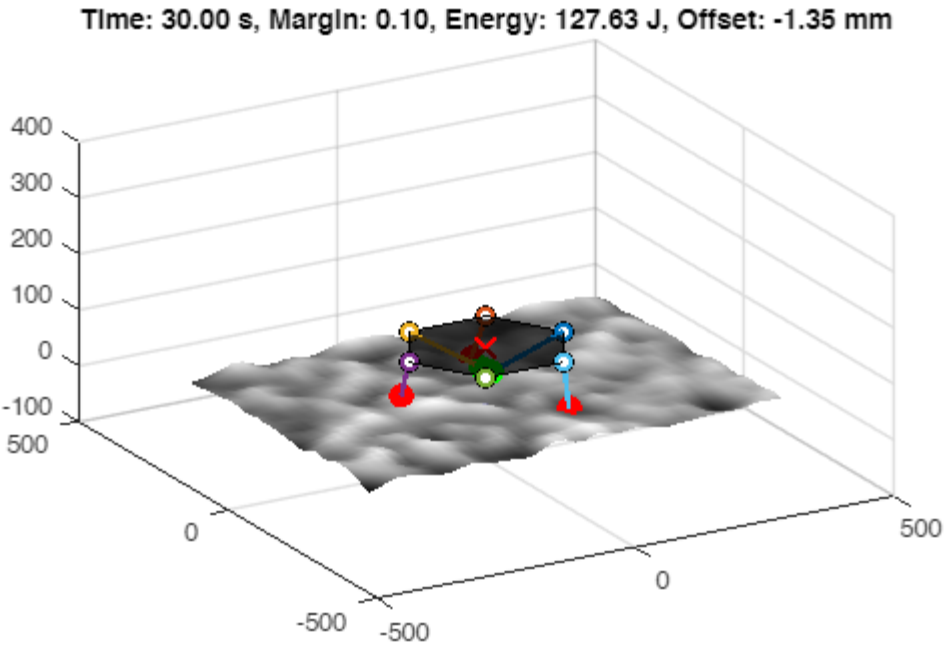

Figure E 17. Hexapod visualization using three-legged gait with fixed legs 1, 3, and 5

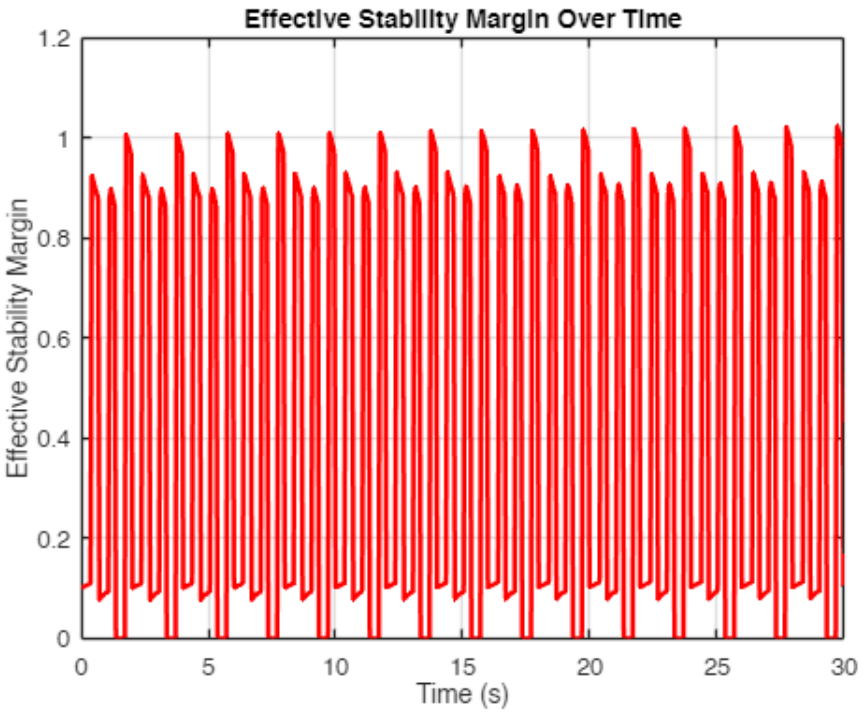

Figure E 18. Effective stability margin over time

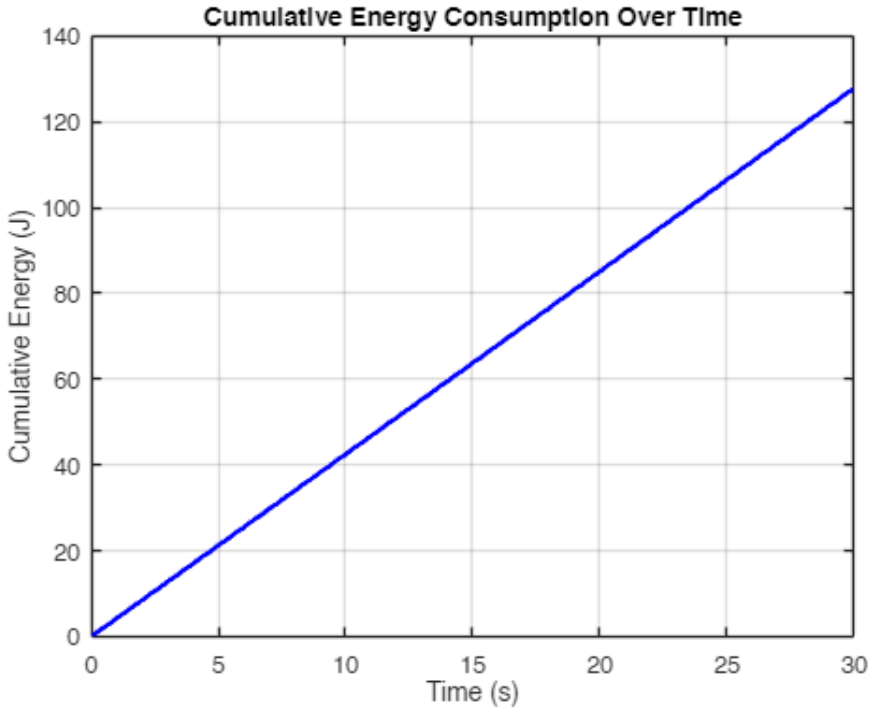

Figure E 19. Cumulative energy consumption over time

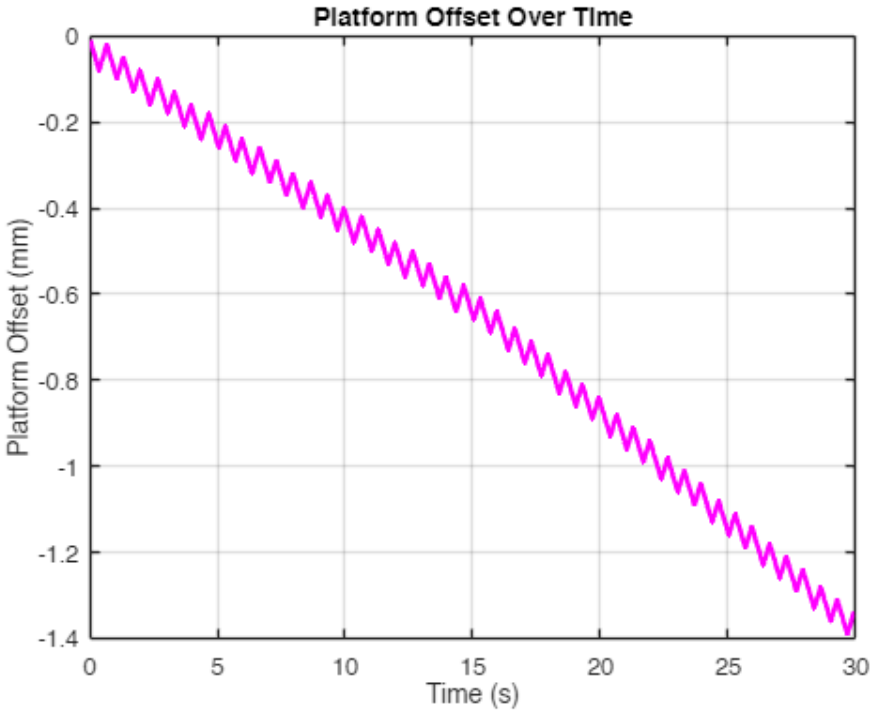

Figure E 20. Platform offset adaptation during the 30-second simulation

E.1.6. Summary of Optimal Gait-Platform Combinations

The table below consolidates the average stability margin, energy consumption, and final platform offset across all evaluated gait configurations:

Table E 1. Summary of gait performance across all simulated scenarios. Metrics include average effective stability margin, total energy consumed over a 30-second simulation period, and the final value of the platform's adaptive vertical offset. Values reflect terrain response and task-based gait constraints.

Scenario	**Avg Stability Margin**	**Energy (J)**	**Final Offset (mm)**
Flat - Ripple	0.57	679.41	−5.49
Inclined - Ripple	0.58	679.41	−5.45
Rough - Wave	0.55	678.90	−5.65
Four-Legged	0.45	134.42	−4.25
Three-Legged	0.40	127.63	−1.35

The ripple gait consistently performed well under flat and inclined terrain, with stable margins near 0.57–0.58 and tightly regulated energy profiles. This reflects its ability to balance ground contact with locomotion efficiency. The wave gait, while energy-efficient on rough terrain, showed lower average stability — a product of terrain unpredictability and slow gait cycles.

Static-load configurations (3- and 4-legged gaits) exhibited drastically lower energy demands but suffered from reduced stability and higher reliance on platform adaptation. The three-legged configuration in particular maintained the lowest offset change but also the narrowest stability margin window. The low offset change recorded for the three-legged and four-legged gaits is due to the decreased initial leg length compared to the rough, inclined and flat.

These patterns highlight the importance of matching gait strategy to terrain conditions and task constraints. Further design implications and trade-offs are examined in Section 6.0.

E.2. Discussions

E.2.1. Gait Performance Trade-offs

The gait selection across scenarios demonstrated clear trade-offs between mechanical efficiency, terrain compliance, and stability margin retention. The ripple gait emerged as a versatile middle ground: it consistently maintained moderate-to-high stability margins while keeping energy consumption tightly regulated. This was particularly evident on flat and inclined terrains, where the staggered swing pattern enabled smoother ground contact transitions and minimized support polygon collapse during leg shifts.

In contrast, the wave gait was implemented on rough terrain due to its inherently conservative structure — maintaining five stance legs at all times. While this configuration minimized sudden margin drops caused by unpredictable terrain elevations, it incurred a cost in locomotion speed and temporal efficiency. Despite that, energy consumption remained comparable to ripple due to fewer abrupt platform corrections and the consistent mechanical cadence of the wave cycle.

The four- and three-legged crawl configurations prioritized energy savings and object stability but showed significantly lower average stability margins. This was expected, as fewer stance permutations reduce the ability to form a robust support polygon. However, their low actuator workload suggests suitability for static payload-carrying tasks where mobility is secondary.

E.2.2. Adaptive Offset Effectiveness

The adaptive platform offset mechanism played a pivotal role in maintaining balance across all terrain scenarios. By dynamically adjusting the vertical position of the hexapod’s centre of mass (CoM), the system compensated for reductions in stability margin without requiring changes in leg coordination or gait timing.

On flat terrain, offset changes were minimal — the platform settled to a low equilibrium early in the simulation and required only small corrections thereafter. This confirmed that under stable conditions, the controller maintained margin without unnecessary actuation, conserving energy.

On inclined terrain, offset adaptation was more active. As the slope angle changed sinusoidally over time, the controller gradually lowered the platform to maintain margin above threshold. This responsiveness enabled ripple gait to remain viable in conditions that would typically destabilize alternating stance gaits like tripod.

Rough terrain triggered the most dynamic offset behaviour. Unpredictable surface elevations caused irregular support patterns, prompting frequent downward adjustments to counteract sudden drops in effective margin. Despite this, the controller prevented instability in all tested runs — even with the more sensitive wave gait.

Notably, the offset mechanism also proved critical in reduced-leg configurations. In both the four- and three-legged crawl gaits, where the system had limited stance options, the adaptive offset provided the only viable method of margin correction. Without it, support failures would have been likely due to poor geometric redundancy.

However, the controller operated purely in the vertical axis. It did not consider lateral tilt or rotational correction, which would be essential in real-world scenarios involving uneven loading or side slopes. This limitation suggests that while the offset strategy is effective, it forms only one component of a more comprehensive terrain-aware control system.

E.2.3. Stability vs. Energy Trade-off

While it is often assumed that higher stability comes at the cost of increased energy consumption, the simulation results revealed a more nuanced relationship. Stability margin and energy usage were not always directly correlated; instead, the interaction between gait dynamics, terrain irregularity, and offset adaptation defined the overall trade-off.

For instance, both the ripple and wave gaits consumed similar amounts of energy (~679 J), despite the wave gait achieving higher peak support margins on rough terrain. This counterintuitive result stems from the fact that wave gait, although slower, requires fewer abrupt corrections — its constant stance phase across five legs ensures smoother platform dynamics and steadier power draw. In contrast, ripple gait introduced more frequent shifts in load distribution, leading to marginally higher correction demands even on flat ground.

Reduced-leg configurations further challenged this trade-off. The three- and four-legged gaits exhibited the lowest energy consumption (127–134 J), yet also the lowest and most erratic stability margins. Their low energy profile was due to the limited number of active swing legs and shorter overall stride cycles — but these benefits were offset by a lack of margin redundancy, making the gait vulnerable to failure without the support of adaptive offset.

Ultimately, the data suggests that while energy and stability are coupled through gait selection and terrain interaction, they do not always move in opposition. Well-tuned coordination — such as ripple on incline or wave on rough ground — can deliver a balance that preserves margin without excessive energy cost, highlighting the importance of terrain-specific gait deployment over universal strategies. This aligns with the findings of Zhai et al. (2020), who demonstrated that gait phase coordination and CoM height adaptation play critical roles in energy optimization across complex terrains.

E.2.4. Implications for Physical Implementation

The simulation findings have clear implications for the practical deployment of hexapod systems in terrain-variable environments. Chief among them is the importance of adaptive gait selection combined with responsive CoM control to maximize terrain survivability without excessive energy penalty.

The ripple gait stands out as a strong candidate for general-purpose locomotion. Its ability to maintain moderate stability margins with consistent energy consumption across flat and inclined terrains suggests it could serve as a default gait in most real-world conditions. However, to translate this into a physical system, gait timing must be tightly coupled with terrain feedback, especially during transitions between level and sloped surfaces.

Wave gait, while slower and more conservative, is a compelling fallback for rough or hazardous terrain. Its higher ground contact ratio reduces the risk of tip-over on uneven substrates — a feature especially useful in search-and-rescue or exploration tasks where footing cannot be guaranteed. Physically, this requires robust synchronization and tolerance to actuator lag, as the gait relies heavily on precise leg phasing.

The role of adaptive offset control in physical hardware is equally critical. Vertical CoM modulation showed measurable impact in all configurations, even when lateral stability was not addressed. To implement this in hardware, a compact but high-torque prismatic mechanism (like the Maxon GP22S drive modelled in simulation) would be necessary, along with real-time feedback from IMUs or force sensors to trigger offset adjustments.

Additionally, the reduced-leg crawl gaits reinforce the importance of task-aware configuration. In manipulation or payload-holding contexts, these gaits enable continued mobility with minimal energy overhead. However, the resulting loss in stability demands compensatory control strategies — potentially including machine learning-based margin prediction or real-time gait switching when terrain conditions deteriorate.

In summary, physical implementation of these findings would benefit most from a modular control system that blends sensor-driven offset control, terrain-aware gait selection, and real-time margin monitoring — ensuring that locomotion is not only efficient, but resilient. This reflects broader trends in autonomous robotics, as discussed by Ting et al. (1994), who emphasized the need for coupling mechanical robustness with adaptive control schemes in terrain-variant locomotion.

E.2.5. Limitations and Future Work

While the simulations offer valuable insight into gait performance, energy efficiency, and terrain adaptability, several limitations must be acknowledged.

Firstly, the analysis was conducted entirely in a simulated environment. While terrain roughness and inclines were modelled with realistic parameters, factors such as actuator backlash, surface friction variability, and mechanical compliance were not included. As such, the results represent idealized performance bounds that may deviate from physical outcomes when deployed on hardware.

Additionally, the platform offset mechanism operated in a simplified vertical-only mode. In real-world applications, maintaining stability often requires multi-axis adaptation, particularly on uneven or laterally sloped terrain. Future implementations should integrate pitch and roll compensation, along with horizontal CoM shifts, to fully stabilize the platform in 3D space.

The current controller also operated without feedback from onboard sensors. Stability margin assessments were derived purely from kinematic calculations, without dynamic force sensing or inertial feedback. Integrating low-cost IMUs, joint torque sensors, or foot force detectors would enable real-time feedback loops, allowing the system to anticipate instability rather than merely react to it.

Furthermore, gait selection in this study was manually assigned per scenario. A more scalable system would involve automated gait switching based on terrain classification or stability margin trends. This could be achieved through reinforcement learning, heuristic rules, or hybrid control architectures.

Lastly, the energy model—though enhanced—relied on idealized motor behaviour and estimated torque curves. A more rigorous approach would involve co-simulation with motor drivers, or hardware-in-the-loop testing to capture efficiency drops under varying loads and real actuator thermal profiles.

These limitations open up several promising avenues for future research, including:

- Deployment on a physical hexapod with full sensory feedback
- Extension to 3D adaptive platform motion (roll, pitch, heave)
- Dynamic gait scheduling based on predictive terrain models
- Integration of force optimization and torque-aware path planning

Such additions would elevate the current system from simulation-driven validation to a deployable autonomous locomotion platform — capable of resilient, terrain-aware navigation under real-world constraints.

The work presented in this report specifically contributes a comparative evaluation of hexapod gait strategies under terrain variation, incorporating adaptive offset mechanics, energy modelling, and reduced-leg configurations. These findings informed broader group decisions regarding gait selection logic, platform stability, and actuator feasibility.

References

Ting, L.H., Blickhan, R. and Full, R.J., 1994. Dynamic and static stability in hexapedal runners. Journal of Experimental Biology, 197(1), pp.251–269.

Zhai, S., Jin, B. and Cheng, Y., 2020. Mechanical design and gait optimization of hydraulic hexapod robot based on energy conservation. Applied Sciences, 10(11), p.3884.